



# Selective hydrogenation of cinnamaldehyde with PtFe<sub>x</sub>/Al<sub>2</sub>O<sub>3</sub>@SBA-15 catalyst: Enhancement in activity and selectivity to unsaturated alcohol by Pt-FeO<sub>x</sub> and Pt-Al<sub>2</sub>O<sub>3</sub>@SBA-15 interaction



Huiyan Pan<sup>a,1</sup>, Junrui Li<sup>a,1</sup>, Jiqing Lu<sup>b</sup>, Guimei Wang<sup>a</sup>, Wenhui Xie<sup>c,\*</sup>, Peng Wu<sup>a</sup>, Xiaohong Li<sup>a,\*</sup>

<sup>a</sup> Shanghai Key Laboratory of Green Chemistry and Chemical Processes, School of Chemistry and Molecular Engineering, East China Normal University, 3663 North Zhongshan Rd., Shanghai 200062, China

<sup>b</sup> Key Laboratory of the Ministry of Education for Advanced Catalysis Materials, Institute of Physical Chemistry, Zhejiang Normal University, Jinhua 321004, China

<sup>c</sup> School of Physics and Materials, East China Normal University, 3663 North Zhongshan Rd., Shanghai 200062, China

## ARTICLE INFO

### Article history:

Received 9 May 2017

Revised 22 July 2017

Accepted 26 July 2017

### Keywords:

Al<sub>2</sub>O<sub>3</sub>@SBA-15 composites

PtFe<sub>x</sub>/Al<sub>2</sub>O<sub>3</sub>@SBA-15 catalysts

Cinnamaldehyde

Selective hydrogenation

Cinnamyl alcohol

## ABSTRACT

Selective hydrogenation of cinnamaldehyde (CAL) to cinnamyl alcohol (COL) was conducted over a series of FeO<sub>x</sub>-doped Pt catalysts supported on a 15 wt% Al<sub>2</sub>O<sub>3</sub>@SBA-15 composite (15AS). It was found that the addition of FeO<sub>x</sub> to the catalyst greatly improved its performance. With an optimal Fe/Pt molar ratio of 0.25, the PtFe<sub>0.25</sub>/15AS catalyst reached a maximum reaction rate (defined as moles of converted CAL per gram of Pt per hour) of 13.93 mol g<sub>Pt</sub><sup>-1</sup> h<sup>-1</sup> with 76.9% selectivity to COL. Additionally, the PtFe<sub>0.25</sub>/15AS catalyst afforded the highest TOF value (defined as moles of converted CAL per mole of Pt active sites per second) of 1.54 s<sup>-1</sup>. X-ray photoelectron spectroscopy analyses and H<sub>2</sub> temperature-programmed reduction and CO diffuse-reflectance infrared Fourier-transformation spectroscopy studies reveal that there is strong interaction between Pt nanoparticles and Al<sub>2</sub>O<sub>3</sub>@SBA-15 composites and also between Pt and FeO<sub>x</sub>, resulting in Pt species with a positive charge being dominant in PtFe<sub>0.25</sub>/15AS catalysts. Therefore, Pt species with positive charges, together with FeO<sub>x</sub> species, are beneficial for preferential adsorption and activation of carbonyl bonds of CAL, so that the activity and selectivity to COL were improved by PtFe<sub>x</sub>/15AS catalysts (*x* represents the Fe/Pt molar ratio).

© 2017 Elsevier Inc. All rights reserved.

## 1. Introduction

Selective hydrogenation of  $\alpha,\beta$ -unsaturated aldehyde for synthesis of  $\alpha,\beta$ -unsaturated alcohols is one of the most atomically efficient routes, in that  $\alpha,\beta$ -unsaturated alcohols are very important intermediates for synthesis of fragrances and pharmaceuticals [1]. However, this reaction is not thermodynamically favored because the C=O bond energy is higher than that of the C=C bond. Nevertheless, efforts have been made in the past two decades to develop efficient catalyst systems. Hydrogenation of cinnamaldehyde (CAL), as a typical  $\alpha,\beta$ -unsaturated aldehyde, is a popularly reported model reaction for the selective activation of C=O or C=C double bonds (Scheme 1) [2–7].

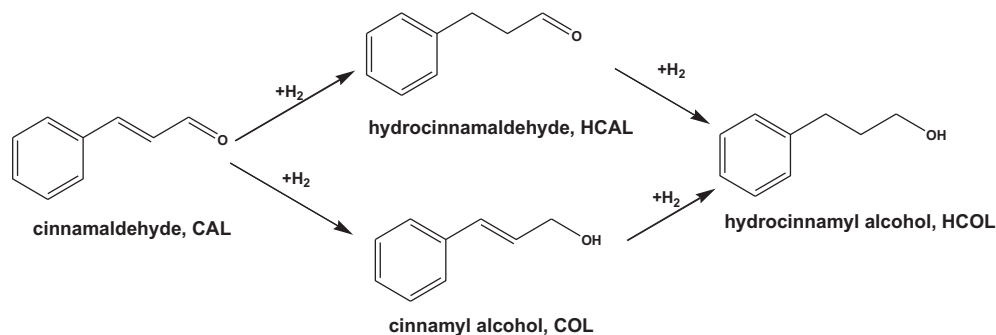
The most commonly used catalysts for the selective hydrogenation of CAL are noble-metal-based catalysts [3–7], among which the Pt-based catalysts have been widely investigated. However, satisfactory selectivity to the desired cinnamyl alcohol (COL) is

often challenging to attain [5]. To improve the performance, particularly the selectivity, various approaches have been developed, which include (1) control of the morphologies of Pt nanoparticles by different synthesis methods [1,8–16]; (2) support-induced modification of Pt properties via strong metal–support interaction (SMSI) [17–24]; (3) Confinement of Pt particles by metal–organic frameworks (MOFs) [25] or surface modification of Pt surface by long-chain ligands [26,27] or thiols [28,29]; (4) addition of promoters such as Zn, Sn, Ge, Fe, Co, or Cu to Pt catalysts [30–41]. Among these approaches, the surface modification strategy can furnish high selectivity to COL, but rather low activity was obtained by a compromise in some cases [26–29]. Additionally, carbon-related materials supported Pt–M catalysts (Pt–Fe [33,34,38,39,41], Pt–Zn [34,39], Pt–Co [36], and Pt–Sn [23]) have shown excellent results including activity and selectivity to COL. This means that the support, the modifier, or the second metal in the supported Pt catalysts would influence the selective hydrogenation of CAL in a combinational manner. The improvement in catalytic performance for the supported Pt catalyst by only one factor seems very limited. Two or more strategies should be adopted to achieve better results, including activity and selectivity to COL.

\* Corresponding authors.

E-mail address: [xhli@chem.ecnu.edu.cn](mailto:xhli@chem.ecnu.edu.cn) (X. Li).

<sup>1</sup> These authors contributed equally to this work.



**Scheme 1.** Selective hydrogenation of CAL.

With regard to support materials for metal catalysts, silica is one of the most commonly used supports for the liquid-phase hydrogenation of CAL [11,16,30,40]. Sometimes Pt catalyst supported on acidic composite oxides, such as SiO<sub>2</sub>-ZrO<sub>2</sub> [24] and CeO<sub>2</sub>-ZrO<sub>2</sub> [21], facilitate hydrogenation of C=O groups in  $\alpha,\beta$ -unsaturated aldehydes. Mesoporous Al<sub>2</sub>O<sub>3</sub>@SBA-15 composites, with a thin layer of amorphous alumina coated on a SBA-15 surface as a kind of special composite oxide, not only retain the mesoporous structure of SBA-15 silica, but also introduce a large number of Lewis acid sites originated from Al<sub>2</sub>O<sub>3</sub>. Moreover, owing to interaction of alumina and silica at the interface, a small number of Brønsted acid sites are also formed in the corresponding Al<sub>2</sub>O<sub>3</sub>@SBA-15 composites. The unique properties of Al<sub>2</sub>O<sub>3</sub>@SBA-15 composites would be inevitably beneficial for interaction of metal and support and thus modulate the electronic properties of metal nanoparticles when used as a support for them. In our preliminary studies, Pt catalyst supported on mesoporous Al<sub>2</sub>O<sub>3</sub>@SBA-15 composites was proved to be active and enantioselective in related asymmetric hydrogenation of  $\alpha$ -ketoesters [42,43].

With these findings in hand, we are motivated to apply Pt or Pt-Fe catalyst supported on mesoporous Al<sub>2</sub>O<sub>3</sub>@SBA-15 composites for the liquid-phase selective hydrogenation of CAL. It is anticipated that there is strong interaction between Pt nanoparticles and Al<sub>2</sub>O<sub>3</sub>@SBA-15 composites and between Pt and Fe; thus the Pt-Fe/Al<sub>2</sub>O<sub>3</sub>@SBA-15 catalyst can exhibit good performance in the liquid-phase hydrogenation of CAL via modulation of the Pt surface electronic state by acidic support and by interaction with the second metal component.

## 2. Experimental

### 2.1. Chemicals

Chloroplatinic acid hexahydrate (H<sub>2</sub>PtCl<sub>6</sub>·6H<sub>2</sub>O) and other chemicals were of analytical grade and used as received. Pluronic 123 (EO<sub>20</sub>PO<sub>70</sub>EO<sub>20</sub>, MW = 5800) was purchased from Sigma-Aldrich. CAL was purchased from Alfa Aesar and was used as received. Other reagents including Fe(NO<sub>3</sub>)<sub>3</sub>·9H<sub>2</sub>O, Al(NO<sub>3</sub>)<sub>3</sub>·9H<sub>2</sub>O, tetraethoxysilane (TEOS), hydrochloric acid (HCl, 37%), and isopropanol were purchased from Sinopharm Chemical Reagent Co., Ltd. and used as received.

### 2.2. Support and catalyst preparation

SBA-15 was prepared according to the method reported in literature [44]. The Al<sub>2</sub>O<sub>3</sub>@SBA-15 mesoporous composite with a Al<sub>2</sub>O<sub>3</sub> content of 15 wt% (denoted as 15AS) was prepared by an ultrasonic impregnation method [42]. The supported Pt/15AS catalyst with a nominal Pt content of 5 wt% was prepared by an incipient wetness impregnation method. Briefly, 2 ml of H<sub>2</sub>PtCl<sub>6</sub> aqueous solution

with a concentration of 14.8 mg Pt/ml was added dropwise to 0.562 g of the 15AS support. The mixture was continuously stirred and then dried in air at ambient temperature. After that, the light yellow solid was calcined in air at 500 °C for 3 h, followed by reduction under H<sub>2</sub> (99.999% purity, 60 ml·min<sup>-1</sup>) at 500 °C for 3 h.

The Fe-doped Pt/15AS catalysts were also prepared in a manner similar to that for the Pt/15AS catalyst, using H<sub>2</sub>PtCl<sub>6</sub> and Fe(NO<sub>3</sub>)<sub>3</sub>·9H<sub>2</sub>O as the precursors. The resulting catalysts, which contained 5 wt% Pt and various Fe contents (0.143 to 1.43 wt%), were denoted as PtFe<sub>x</sub>/15AS, where *x* referred to the Fe/Pt molar ratio. Correspondingly, the *x* value varied from 0.1 to 1.

### 2.3. Catalyst characterizations

X-ray diffraction (XRD) patterns of the samples were collected using a Bruker D8 Advance instrument, using CuK $\alpha$  radiation. Nitrogen adsorption-desorption isotherms were measured at -196 °C (77 K) using a Quantachrome Autosorb-3B system after the samples were evacuated at 200 °C for 10 h. The Brunauer-Emmet-Teller (BET) specific surface area was calculated using an adsorption branch recorded in the relative pressure range from 0.05 to 0.35. The pore size distribution curves were calculated via analysis of the adsorption branch of the isotherm, using the Barrett-Joyner-Halenda (BJH) algorithm. Scanning electron microscopy (SEM) images were taken on a Hitachi S4800 electron microscope with an acceleration voltage of 20 kV. Transmission electron microscopy (TEM) images were recorded with a JEM-2100F microscope with a field emissive gun, operated at 200 kV and with a point resolution of 0.24 nm. Before measurements, the samples were dispersed in ethanol under sonication and dropped onto a copper grid to take TEM images.

X-ray photoelectron spectroscopy (XPS) measurements were performed using a Thermo Fisher Scientific ESCALAB 250Xi spectrometer with an AlK $\alpha$  radiation (1486.6 eV) incident beam. The sample was pretreated in situ for 2 h under high-purity hydrogen (>99.999%, 30 ml min<sup>-1</sup>) at 400 °C in a reactor attachment of the XPS spectrometer. The binding energy (BE) was calibrated using C-C binding energy at 284.4 eV in order to compare the BE with the data from the literature. The spectra shown in the figures have been corrected by subtraction of a Shirley background. Spectral fitting and peak integration were done using XPSPEAK software.

CO chemisorption on the catalysts was performed by diffuse-reflectance infrared Fourier-transformation spectroscopy (DRIFTS). The catalyst was pretreated in a H<sub>2</sub> flow (99.999% purity, 40 ml min<sup>-1</sup>) at 400 °C for 2 h before CO adsorption at 35 °C. After the adsorption of CO, the sample was purged with N<sub>2</sub> (99.999% purity, 40 ml min<sup>-1</sup>) at 35 °C for 1 h. All of the IR spectra were collected using 64 scans at a resolution of 4 cm<sup>-1</sup>.

The H<sub>2</sub> temperature-programmed reduction (TPR) technique was employed to analyze the reducibility of the catalyst using Micromeritics AutoChem II Chemisorption Analyzer. A sample of

50 mg of the as-prepared (calcined) catalyst was placed in a quartz reactor and pretreated in a He flow (99.999% purity, 20 ml min<sup>-1</sup>) at 300 °C for 60 min in order to remove the adsorbed water and carbonates, and then the sample was cooled to 40 °C in a He flow (99.999% purity, 20 ml min<sup>-1</sup>). After that, the sample was heated from 40 to 700 °C at 10 °C min<sup>-1</sup> under a mixture of 10% H<sub>2</sub>-Ar (20 ml min<sup>-1</sup>). The rate of H<sub>2</sub> consumption was monitored by a gas chromatograph (GC) with a thermal conductivity detector (TCD).

#### 2.4. Catalytic test

The catalysts were tested for the liquid-phase hydrogenation of CAL in a 100 mL autoclave. For a typical test, 50 mg of the catalyst was pretreated in a specially designed quartz tube under H<sub>2</sub> (99.999% purity, 40 ml min<sup>-1</sup>) at 400 °C for 2 h before use. Then the pretreated catalyst was immediately transferred into the autoclave without exposure to air and mixed with solvent (containing isopropanol and water with a volume ratio of 9:1) and CAL. The reaction began when hydrogen (2.0 MPa, 99.999% purity) was introduced with stirring at 90 °C (1200 rpm). The reaction was stopped after a proper time and the products were analyzed using a GC (GC-2014, Shimadzu) equipped with a flame ionization detector (FID) and a capillary column (DM-WAX, 30 m × 0.32 mm × 0.25 μm). The response factor of each component was calculated using standard samples and was used to calculate the conversion and selectivity.

It should be pointed out that the absence of internal and external mass transfer limitations in the reaction was verified by the Weisz–Prater criterion and the Mears criterion, respectively. The absence of heat transfer limitation in the reaction was verified by a Mears criterion [45]. At the maximum conversion,  $C_{WP} = 6.37 \times 10^{-6} < 1$  and  $C_M = 0.0498 < 0.15$ , which ensured the absence of a mass transfer limitation. The Mears criterion for external

(interphase) heat transfer gave  $\left| \frac{-\Delta H_r(-r_A')\rho_b R E}{h_i T_b^2 R_g} \right| < 0.15$ , demonstrating no heat transfer limitations. The influence of the stirring rate on catalytic performance was also investigated to make sure that the hydrogenation reaction was out of the diffusion control zone (see the Supporting Information for the details).

### 3. Results and discussion

#### 3.1. Selective hydrogenation of CAL over various Pt catalysts

First, we investigated Pt catalysts supported on different materials including pristine SBA-15 silica, Al<sub>2</sub>O<sub>3</sub>, and 15AS for the liquid-phase hydrogenation of CAL. Table 1 lists the detailed results for the liquid-phase hydrogenation of CAL over Pt/SBA-15, Pt/15AS, and a commercial Pt/Al<sub>2</sub>O<sub>3</sub> catalyst. The Pt/SBA-15 catalyst gives a CAL conversion of 22.3% and a COL selectivity of 40.9%. Besides COL, the products also contain HCAL (hydrocinnamaldehyde) and HCOL (hydrocinnamyl alcohol). The commercial Pt/Al<sub>2</sub>O<sub>3</sub> catalyst gives similar CAL conversion, but the COL selectivity afforded by this catalyst is considerably higher (63.7%). For the Pt/15AS catalyst, a COL conversion of 34.9% and a COL selectivity of 64.7% are obtained. That is, the Pt nanoparticles supported on 15AS composites show better results for the liquid-phase hydrogenation of CAL.

To explain the enhanced performance of the Pt/15AS catalyst, the relevant Pt catalysts were characterized using SEM, XRD, and TEM. The morphology of the 15AS composite was characterized using SEM (Fig. 1). Amorphous alumina is uniformly dispersed along the mesoporous channels and outside the mesopores of the SBA-15 host, and no obvious needlelike crystalline alumina is observed. The mesoporous structure of 15AS was also characterized by the low-angle XRD patterns. As displayed in Fig. 2A, similarly to the SBA-15 host, the 15AS support and the Pt/15AS catalyst exhibit an intense diffraction peak and two weak peaks,

**Table 1**  
Reaction results of CAL hydrogenation with different Pt catalysts.<sup>a</sup>

Entry	Catalyst	Fe loading (wt.%)	Fe/Pt molar ratio (x)	Pt particle size (nm) <sup>b</sup>	Dispersion (%) <sup>c</sup>	Conv. (%)	TOF (s <sup>-1</sup> ) <sup>d</sup>	Selectivity (%)		
								COL	HCAL	HCOL
1	Pt/SBA-15	0	0	6.5	17.4	22.3	0.21	40.9	46.3	12.8
2	Pt/Al <sub>2</sub> O <sub>3</sub> <sup>e</sup>	0	0	3.1	36.8	21.9	0.10	63.7	27.7	8.5
3	Pt/15AS	0	0	5.3	21.3	34.9	0.27	64.7	26.8	8.5
4	PtFe <sub>0.10</sub> /15AS	0.143	0.10	1.8	62.8	61.8	0.48	72.3	20.9	6.7
5	PtFe <sub>0.15</sub> /15AS	0.215	0.15	2.3	49.1	60.2	0.59	71.4	22.9	5.7
6	PtFe <sub>0.20</sub> /15AS	0.287	0.20	2.5	45.2	61.5	0.66	78.9	15.4	5.7
7 <sup>f</sup>	PtFe <sub>0.25</sub> /15AS	0.359	0.25	2.3	49.1	77.4	1.54	76.9	15.2	7.8
8 <sup>g</sup>	PtFe <sub>0.25</sub> /15AS	0.359	0.25	2.3	49.1	44.4	0.44	80.9	15.1	4.0
9 <sup>h</sup>	PtFe <sub>0.25</sub> /15AS	0.359	0.25	2.3	49.1	77.0	1.53	75.7	15.6	8.6
10 <sup>i</sup>	PtFe <sub>0.25</sub> /15AS	0.359	0.25	2.3	49.1	76.2	1.51	76.2	15.4	8.3
11	PtFe <sub>0.3</sub> /15AS	0.430	0.30	n.m. <sup>j</sup>	n.m. <sup>j</sup>	60.1	—	81.0	13.8	5.2
12	PtFe <sub>0.45</sub> /15AS	0.650	0.45	n.m. <sup>j</sup>	n.m. <sup>j</sup>	31.2	—	82.2	14.2	3.6
13	PtFe <sub>1</sub> /15AS	1.43	1.0	n.m. <sup>j</sup>	n.m. <sup>j</sup>	15.5	—	91.2	8.9	2.8
14 <sup>k</sup>	PtFe <sub>1</sub> /15AS	1.43	1.0	n.m. <sup>j</sup>	n.m. <sup>j</sup>	27.0	—	81.0	17.0	3.0
15 <sup>f</sup>	PtFe <sub>0.25</sub> /SBA-15	0.359	0.25	n.m. <sup>j</sup>	n.m. <sup>j</sup>	25.4	—	90.9	7.7	1.4
16	PtFe <sub>0.25</sub> /SBA-15	0.359	0.25	n.m. <sup>j</sup>	n.m. <sup>j</sup>	46.2	—	75.1	22.0	2.9

<sup>a</sup> Reaction conditions: 50 mg catalyst, 7.5 mmol CAL (for entries 1–3) and 22.5 mmol CAL (for entries 4–16), 18 mL isopropanol and 2 mL water, 2 MPa H<sub>2</sub>, 90 °C, 1 h, 1200 rpm. COL represents cinnamyl alcohol, HCAL represents hydrocinnamaldehyde, and HCOL represents hydrocinnamyl alcohol.

<sup>b</sup> Pt particle size was calculated from the TEM images.

<sup>c</sup> Dispersion was calculated based on dispersion (%) × d (Pt particle size in nm) = 1.13.

<sup>d</sup> TOF value was defined as the number of moles of converted CAL per mole of Pt active sites per second.

<sup>e</sup> 5 wt% Pt/Al<sub>2</sub>O<sub>3</sub> catalyst was purchased from Alfa Aesar.

<sup>f</sup> 0.5 h.

<sup>g</sup> 25 °C, 1 h.

<sup>h</sup> 1 MPa H<sub>2</sub>, 0.5 h.

<sup>i</sup> 1 bar H<sub>2</sub>, 0.5 h.

<sup>j</sup> Not measured.

<sup>k</sup> 2 h.

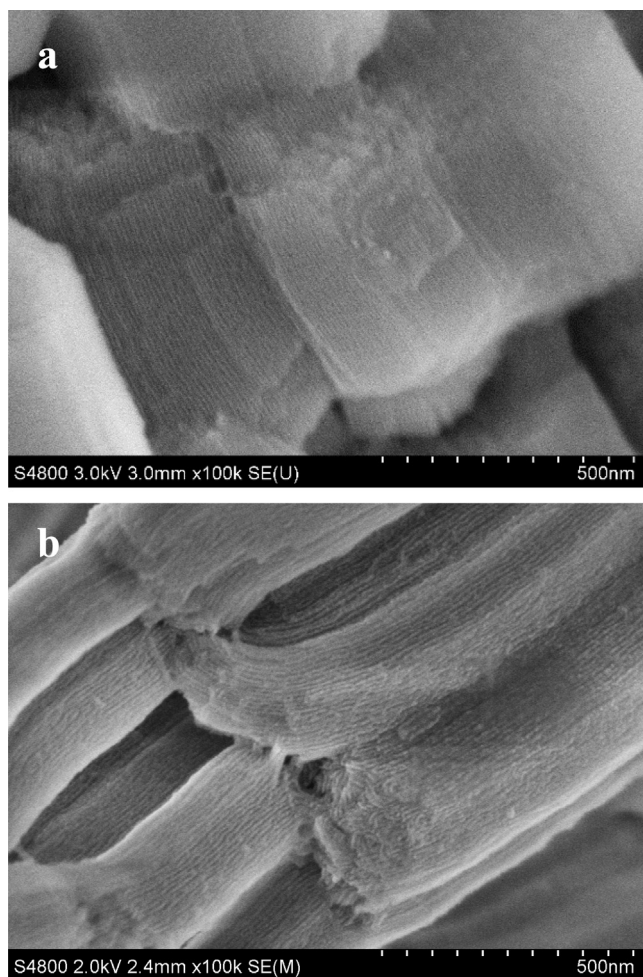


Fig. 1. SEM images of (a) SBA-15 and (b) 15AS.

attributed to the (1 0 0), (1 1 0), and (2 0 0) planes of the hexagonal structure ( $P6mm$ ), respectively [44]. The difference in peak intensity might be caused by different sample thicknesses for XRD measurement. The Pt crystallites of the catalysts were characterized using wide-angle XRD as well. As can be seen in Fig. 2B, the Pt/SBA-15 catalyst shows three sharp diffraction peaks at  $2\theta$  of  $39.8^\circ$ ,  $46.4^\circ$ , and  $67.6^\circ$ , assigned to the Pt(1 1 1), Pt(2 0 0), and Pt(2 2 0) planes, respectively. After alumina was coated onto SBA-15 to form 15AS composites, the diffraction of Pt crystallite for the Pt/15AS catalyst became broader. As for the commercial Pt/ $\text{Al}_2\text{O}_3$  catalyst, it shows extremely weak diffraction. This indicates that the commercial Pt/ $\text{Al}_2\text{O}_3$  catalyst has quite small Pt particles, while the Pt/SBA-15 catalyst has relatively larger Pt particles. The Pt catalysts were also characterized using TEM and the Pt particle size distribution was calculated accordingly (Figs. S2 and S3 in the Supporting Information and Fig. 3). As listed in Table 1 as well, the average Pt particle sizes for the Pt/SBA-15, Pt/15AS, and Pt/ $\text{Al}_2\text{O}_3$  catalysts center at 6.5, 5.3, and 3.1 nm, respectively. Correspondingly, turnover frequency (TOF, the number of moles of converted CAL per mole of Pt active sites per second) based on surface Pt atoms was also calculated and listed in Table 1. The Pt/SBA-15, Pt/ $\text{Al}_2\text{O}_3$ , and Pt/15AS afford TOF values of 0.21, 0.10, and  $0.27\text{ s}^{-1}$ , respectively.

The enhanced performance of the Pt/15AS catalyst suggests a positive role of the support in the reaction, which is probably due to the presence of Lewis acidic sites in the support [11,21,24,43]. Additionally, we deduce that the interaction of Pt nanoparticles with  $\text{Al}_2\text{O}_3$ @SBA-15 composites can modulate the

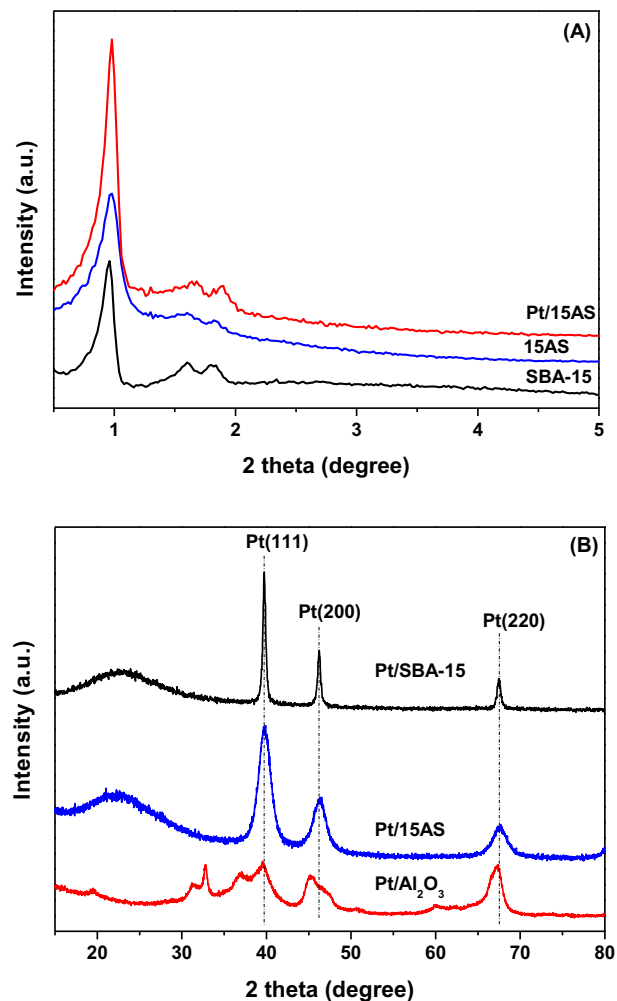


Fig. 2. (A) Low-angle XRD patterns of SBA-15, 15AS and Pt/15AS catalyst and (B) wide-angle XRD patterns of Pt/SBA-15, Pt/15AS and commercial Pt/ $\text{Al}_2\text{O}_3$  catalysts.

surface properties of Pt nanoparticles, so that both the activity and selectivity to COL are promoted after Pt nanoparticles are loaded onto the composite materials. Nevertheless, improvement is still very limited at this stage.

### 3.2. Selective hydrogenation of CAL over $\text{FeO}_x$ -promoted Pt/15AS catalysts

To further improve the performance of the Pt/15AS catalyst, Fe-doped  $\text{PtFe}_x/15\text{AS}$  catalysts were employed for this reaction. It should be noted that owing to higher activity after Fe addition to the Pt/15AS catalyst, the hydrogen consumption was too fast to control the reaction so, we added three times as much CAL to carry out the reaction with the  $\text{PtFe}_x/15\text{AS}$  catalysts. In addition, the reaction time was also shortened to one-half according to hydrogen consumption for the  $\text{PtFe}_{0.25}/15\text{AS}$  catalyst.

As summarized in Table 1, with addition of trace amounts of Fe to the Pt/15AS catalyst, the catalytic performance, especially for the conversion of CAL, is significantly enhanced. As a result, the  $\text{PtFe}_{0.10}/15\text{AS}$  catalyst shows 61.8% conversion of CAL and 72.3% selectivity to COL. With Fe/Pt molar ratio  $x$  increasing from 0.10 to 0.20, the activities of the catalysts remain almost constant. When the  $x$  value increases to 0.25, the  $\text{PtFe}_{0.25}/15\text{AS}$  catalyst gives a CAL conversion of 77.4% and a COL selectivity of 76.9% within a half reaction time. However, when the Fe/Pt molar ratio  $x$  is further increased from 0.30 to 1, the CAL conversion declines instead,

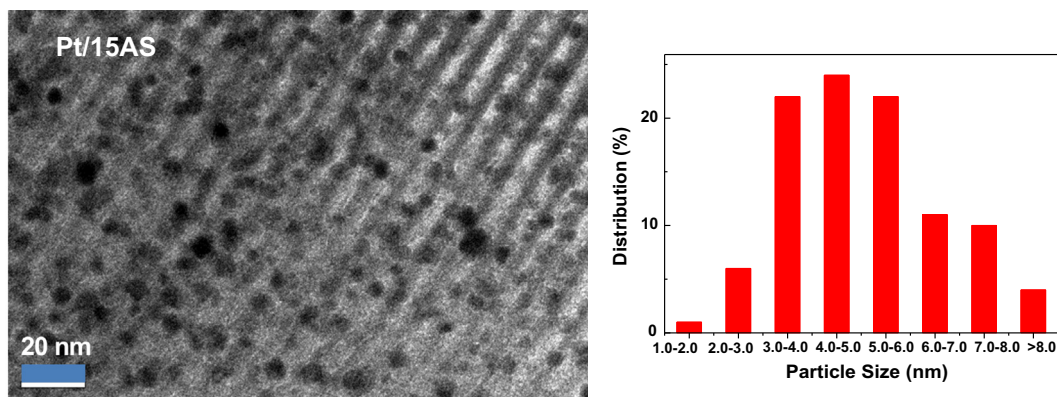


Fig. 3. TEM image and particle size distribution of Pt/15AS.

although the COL selectivity increases slightly. As a result, the PtFe<sub>1.0</sub>/15AS catalyst with the highest Fe/Pt molar ratio of 1.0 only converts 15.5% of CAL under the same conditions, although the selectivity to COL reached a maximum of 91.2%.

In order to make clear the changing selectivity, the hydrogenation of CAL with the PtFe<sub>1.0</sub>/15AS catalyst was prolonged to 2 h. To our disappointment, although the CAL conversion increased to 27.0%, the selectivity to COL decreased dramatically to 81.0%. Nevertheless, the selectivity to HCOL did not increase, while the selectivity to HCAL increased obviously. This is a very common phenomenon in the selective hydrogenation of CAL [14,22,26,37].

For clarity, we correlated the mass-specific rates of CAL consumption ( $MSA_{CAL}$ ) (defined as the moles of converted CAL per gram of Pt per hour) and COL formation ( $MSA_{COL}$ ) (defined as the moles of formed COL per gram of Pt per hour) with the Fe/Pt molar ratio  $x$  in PtFe <sub>$x$</sub> /15AS catalysts. As shown in Fig. 4, the  $MSA_{CAL}$  greatly increased from 1.05 mol g<sub>Pt</sub><sup>-1</sup> h<sup>-1</sup> for the Pt/15AS catalyst to 5.56 mol g<sub>Pt</sub><sup>-1</sup> h<sup>-1</sup> for the PtFe<sub>0.10</sub>/15AS catalyst. The highest  $MSA_{CAL}$  of 13.93 mol g<sub>Pt</sub><sup>-1</sup> h<sup>-1</sup> was obtained with the PtFe<sub>0.25</sub>/15AS catalyst with a COL selectivity of 76.9%. However, when the Fe/Pt molar ratio  $x$  further increased, the  $MSA_{CAL}$  declined. That is, for Fe/Pt with an optimal molar ratio, the  $MSA_{CAL}$  is increased by almost 13 times for the bimetallic PtFe<sub>0.25</sub>/15AS catalyst in comparison with the monometallic Pt/15AS catalyst. Similarly, the

$MSA_{COL}$  versus Fe/Pt molar ratio  $x$  also displays a volcano-like curve and the highest  $MSA_{COL}$  of 10.71 mol g<sub>Pt</sub><sup>-1</sup> h<sup>-1</sup> is furnished by the PtFe<sub>0.25</sub>/15AS catalyst (see the inset of Fig. 4).

The reusability of the PtFe <sub>$x$</sub> /15AS was also investigated. As displayed in Fig. 5, the PtFe<sub>0.25</sub>/15AS catalyst can be recovered easily by filtration and recycled just by washing with fresh solvent three times. Consequently, the PtFe<sub>0.25</sub>/15AS catalyst can be reused at least six times without obvious loss in activity or selectivity to COL. We also detected the Pt leaching amount in the filtrate, and to our delight, the PtFe<sub>0.25</sub>/15AS catalyst is very stable and the leached Pt amount is below the ICP-AES detection limit.

Based on these results, the catalytic performance of PtFe <sub>$x$</sub> /15AS was greatly enhanced over that of Pt/15AS. Furthermore, among all of the PtFe <sub>$x$</sub> /15AS catalysts, the PtFe<sub>0.25</sub>/15AS catalyst affords the highest  $MSA_{CAL}$  and  $MSA_{COL}$ . Of particular note is that the PtFe<sub>0.25</sub>/15AS catalyst can easily be recovered and recycled.

To understand the difference between PtFe <sub>$x$</sub> /15AS catalysts with different Fe/Pt molar ratios, the PtFe <sub>$x$</sub> /15AS catalysts were characterized using some general techniques. As already mentioned, the low-angle XRD patterns indicate that the 15AS support and the Pt/15AS catalyst reserve the mesostructure of the SBA-15 host. The well-ordered mesoporous structures of the 15AS support, the Pt/15AS, and the PtFe <sub>$x$</sub> /15AS catalysts were further confirmed by N<sub>2</sub> sorption (Fig. 6). All the samples show typical type IV hysteresis

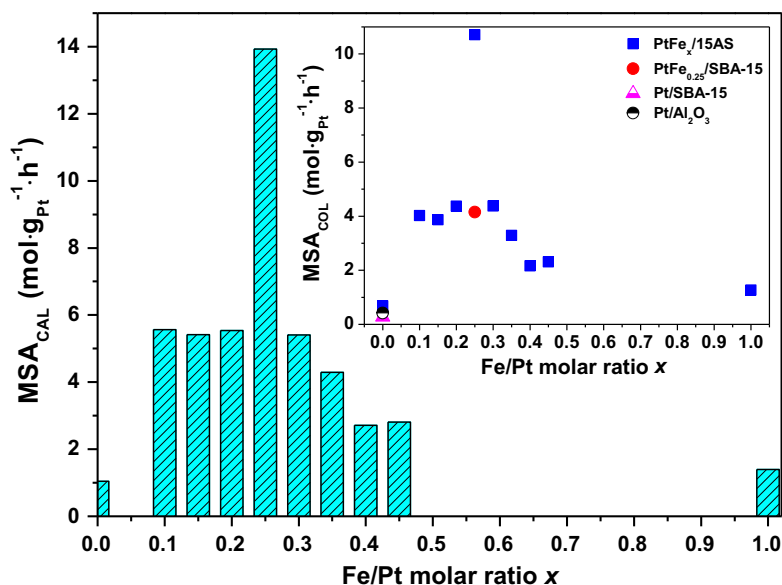


Fig. 4. Mass-specific rate of CAL consumption ( $MSA_{CAL}$ ) and COL formation ( $MSA_{COL}$ ) vs. the Fe/Pt molar ratio  $x$  in the PtFe <sub>$x$</sub> /15AS catalysts.

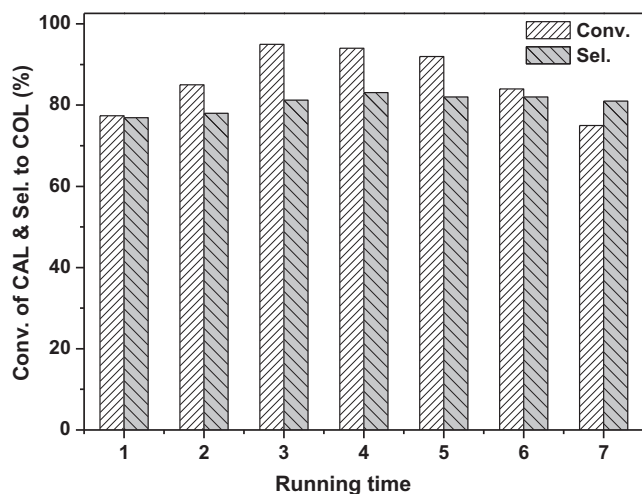


Fig. 5. The reusability of the  $\text{PtFe}_{0.25}/15\text{AS}$  catalyst for the hydrogenation of CAL. The reaction conditions are the same as those for entry 7, Table 1.

loops in the relative pressure range from 0.35 to 0.80, demonstrating that the mesoporous structure of the SBA-15 host is still maintained even after loading of alumina or Pt nanoparticles. However, the BET specific surface area and pore volume calculated per g of SBA-15 decrease after the loading of alumina. As listed in Table 2, compared with that of the SBA-15 host, the BET specific surface area of the 15AS decreases from 768 to  $493 \text{ m}^2 \text{ g}^{-1}$  and the pore volume decreases to  $0.82 \text{ cm}^3 \text{ g}^{-1}$ . The average pore size of the 15AS is 7.8 nm, which is slightly smaller than that of the SBA-15 host (8.0 nm). Moreover, the loading of Pt nanoparticles in the catalyst results in a further decline in the BET specific surface area ( $419 \text{ m}^2 \text{ g}^{-1}$ ) and pore volume ( $0.66 \text{ cm}^3 \text{ g}^{-1}$ ), while the addition of Fe with Fe/Pt molar ratio  $x$  varying from 0.10 to 1.0 in the catalyst hardly changes the physicochemical properties, with the BET specific surface area ranging from 409 to  $425 \text{ m}^2 \text{ g}^{-1}$  and the pore volume ranging from 0.57 to  $0.69 \text{ cm}^3 \text{ g}^{-1}$ . That is, although addition of  $\text{FeO}_x$  to Pt/15AS catalysts causes a decrease in BET specific surface area and pore volume, the differences in those physicochemical parameters of the  $\text{PtFe}_x/15\text{AS}$  catalyst with various Fe/Pt ratios are negligible, while the catalytic performance of the

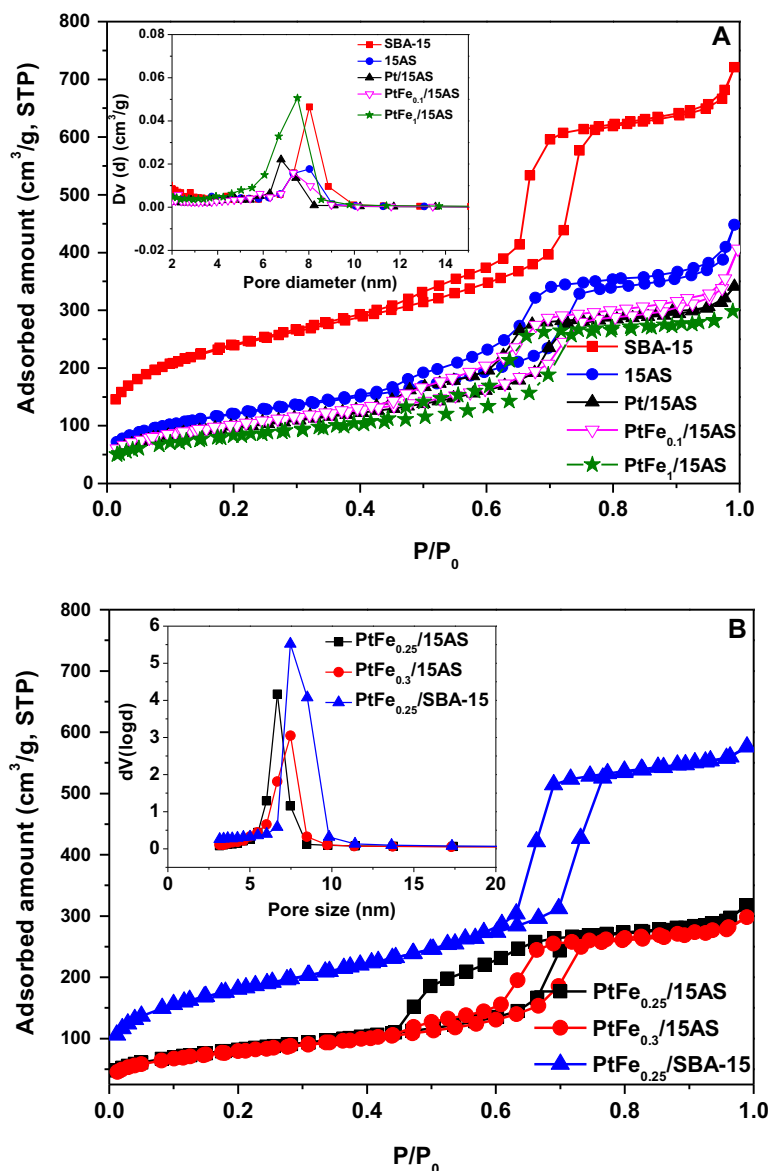


Fig. 6.  $\text{N}_2$  adsorption–desorption isotherms and pore size distributions (inset) of (A) SBA-15, 15AS, Pt/15AS,  $\text{PtFe}_{0.1}/15\text{AS}$ , and  $\text{PtFe}_1/15\text{AS}$  and (B)  $\text{PtFe}_{0.25}/15\text{AS}$ ,  $\text{PtFe}_{0.3}/15\text{AS}$ , and  $\text{PtFe}_{0.25}/\text{SBA-15}$ .

**Table 2**  
Physicochemical parameters of SBA-15, 15AS, and the related catalysts.

Entry	Sample	$S_{\text{BET}}$ ( $\text{m}^2 \text{g}^{-1}$ ) <sup>a</sup>	$V_p$ ( $\text{cm}^3 \text{g}^{-1}$ ) <sup>a</sup>	$D_p$ (nm)
1	SBA-15	768	1.02	8.0
2	15AS	493	0.82	7.8
3	Pt/15AS	419	0.66	6.9
4	PtFe <sub>0.10</sub> /15AS	425	0.69	7.3
5	PtFe <sub>0.25</sub> /15AS	418	0.61	6.8
6	PtFe <sub>0.30</sub> /15AS	409	0.57	7.4
7	PtFe <sub>1</sub> /15AS	420	0.59	7.5
8	PtFe <sub>0.25</sub> /SBA-15	668	0.94	7.5

<sup>a</sup> The BET specific surface area and pore volume were calculated per g of SBA-15.

PtFe<sub>x</sub>/15AS catalysts is dramatically influenced by the Fe/Pt molar ratio. Therefore, the difference in physicochemical properties is not the key factor that affects the catalytic performance.

The Pt crystallite in the PtFe<sub>x</sub>/15AS catalysts was also characterized using wide-angle XRD. As displayed in Fig. 7, with addition of FeO<sub>x</sub>, the Pt(1 1 1) diffraction at  $2\theta$  of 39.8° for the PtFe<sub>0.10</sub>/15AS catalyst is dramatically suppressed, indicating that addition of a trace amount of FeO<sub>x</sub> is very beneficial for the dispersion of Pt nanoparticles. With increasing FeO<sub>x</sub> amount, the PtFe<sub>0.15</sub>/15AS, PtFe<sub>0.20</sub>/15AS, and PtFe<sub>0.25</sub>/15AS catalysts give weak diffraction peaks as well. If the FeO<sub>x</sub> amount is further increased, the PtFe<sub>x</sub>/15AS catalyst ( $x \geq 0.30$ ) shows a very strong Pt(1 1 1) diffraction peak, demonstrating that large Pt crystallites are formed.

The TEM images of some representative catalysts are shown in Fig. 8, as well as the Pt particle size distributions. As already discussed in the previous section, the Pt/15AS catalyst shows a broad Pt particle size distribution, ranging from 1.0 to 8.0 nm and centering at 3.0–6.0 nm (Fig. 3). After the FeO<sub>x</sub> doping, the Pt particles in the PtFe<sub>0.10</sub>/15AS, PtFe<sub>0.20</sub>/15AS, and PtFe<sub>0.25</sub>/15AS catalysts become smaller and more uniform than those in the Pt/15AS catalyst, with Pt particle sizes ranging from 2.0 to 4.0, 2.0 to 4.0, and 1.5 to 3.0 nm, respectively. As for the PtFe<sub>0.30</sub>/15AS catalyst, the Pt particles are not uniformly dispersed; some Pt particles are well

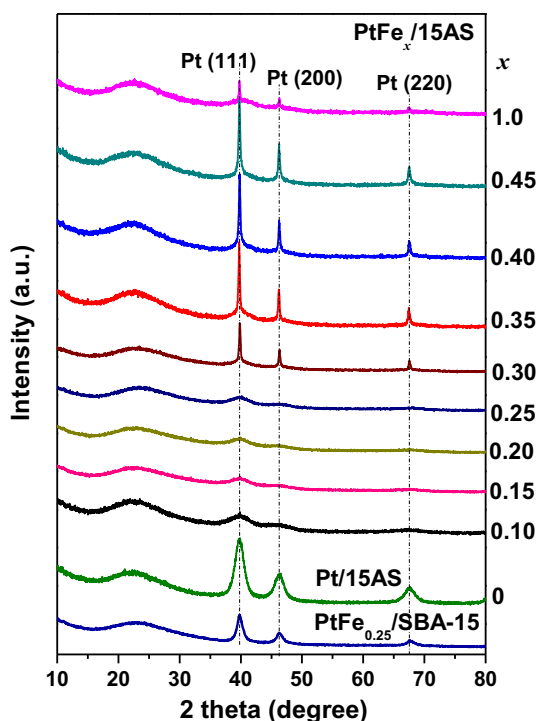


**Fig. 7.** Wide-angle XRD patterns of PtFe<sub>x</sub>/15AS catalysts and PtFe<sub>0.25</sub>/SBA-15 catalyst.

dispersed while others aggregate to form very large and perfect cubic crystallite (see Fig. S4 in the Supporting Information). These results agree well with the XRD results. It is clear that the addition of a small amount of FeO<sub>x</sub> (Fe/Pt  $\leq 0.25$ ) in the Pt/15AS catalyst leads to smaller Pt size (1.8–2.5 nm) compared with the bare Pt/15AS (5.3 nm), while a large amount of FeO<sub>x</sub> (Fe/Pt  $> 0.25$ ) results in large Pt particles ( $> 10$  nm). In some cases, the average Pt particle size calculated from the Scherrer equation is larger than 20 nm, indicating that the Pt nanoparticles are located on the outer surface of 15AS. Thus, the different Pt particle sizes for the PtFe<sub>x</sub>/15AS catalysts with variable Fe/Pt molar ratio might play an important role in determining the catalytic performance. Nevertheless, when the Fe/Pt molar ratio is lower than 0.25, the PtFe<sub>x</sub>/15AS catalysts still furnish rather different results, although they have similar Pt particle sizes. Hence, the Pt particle size is not the only factor influencing the catalytic performance.

Besides, on recalling the performance of Pt/SBA-15, Pt/15AS, and PtFe<sub>x</sub>/15AS catalysts, we find that the performance of Pt catalyst is significantly improved after Al<sub>2</sub>O<sub>3</sub> is added to the support and particularly after Fe is doped. Addition of alumina to the support can certainly be beneficial to dispersion of Pt particles due to interaction of Pt with alumina. Additionally, coating of SBA-15 with alumina forms a large amount of Lewis acid, which is helpful for selective adsorption of C=O double bonds [21,24]. Furthermore, doping of Fe with low content also greatly enhances the catalytic performance, indicating that there is strong interaction between Pt and FeO<sub>x</sub>. In comparison, the PtFe<sub>0.25</sub>/15AS catalyst shows superior performance for the tested reaction. This could be ascribed to two reasons. The first is that Pt nanoparticles for the PtFe<sub>0.25</sub>/15AS catalyst can disperse very well on the support, which can be confirmed from the XRD pattern and TEM image (Figs. 7 and 8). The second reason might be that the PtFe<sub>0.25</sub>/15AS catalyst has optimal surface electronic properties, which need further characterization.

### 3.3. Further investigation and discussion

Before thoroughly characterizing the PtFe<sub>x</sub>/15AS catalysts using special spectroscopic and temperature-programmed techniques, we want to compare the results in this case with the literature in advance. Additionally, the catalytic performance of the PtFe<sub>x</sub>/15AS catalysts, especially the outstanding PtFe<sub>0.25</sub>/15AS catalyst, should be further explored to the greatest extent under milder conditions.

As discussed above, our findings suggest that an optimal Fe/Pt ratio is crucial for the catalytic performance, which is in accordance with observations in the literature. For instance, Neri et al. [46] investigated zeolite P-supported Pt–Fe catalysts for the selective liquid-phase hydrogenation of CAL. They found that the highest COL selectivity of 85% at 90% CAL conversion was obtained at a Pt/Fe weight ratio of 1, and the selectivity decreased with further increase in the Fe amount. However, the authors did not discuss the reasons. Very recently, Shi et al. [47] found that Fe/Pt molar ratios of 0.2–0.25 were optimal for the selective hydrogenation of CAL over Pt–FeO<sub>x</sub>/SiO<sub>2</sub> catalysts prepared by a galvanic displacement method, in good accord with our observations. Besides, it is worth noting that, in our case, the PtFe<sub>x</sub>/15AS catalysts have much higher reaction rates (including  $MSA_{\text{CAL}}$  and  $MSA_{\text{COL}}$ ) than those reported in the literature. The highest  $MSA_{\text{CAL}}$  of 13.93 mol g<sub>Pt</sub><sup>-1</sup> h<sup>-1</sup> (with the highest  $MSA_{\text{COL}}$  of 10.71 mol g<sub>Pt</sub><sup>-1</sup> h<sup>-1</sup>) obtained with the PtFe<sub>0.25</sub>/15AS catalyst in our case is much higher than those achieved with similar Pt–FeO<sub>x</sub>/SiO<sub>2</sub> catalysts, which furnished the highest  $MSA_{\text{CAL}}$  of 2.24 mol g<sub>Pt</sub><sup>-1</sup> h<sup>-1</sup> and the highest  $MSA_{\text{COL}}$  of less than 2 mol g<sub>Pt</sub><sup>-1</sup> h<sup>-1</sup> [47].

In addition, the role of the Al<sub>2</sub>O<sub>3</sub>@SBA-15 composite (15AS) was also emphasized by comparing the performance of the PtFe<sub>0.25</sub>/15AS and PtFe<sub>0.25</sub>/SBA-15 catalysts prepared by the same method. As listed in Table 2, the PtFe<sub>0.25</sub>/SBA-15 catalyst shows

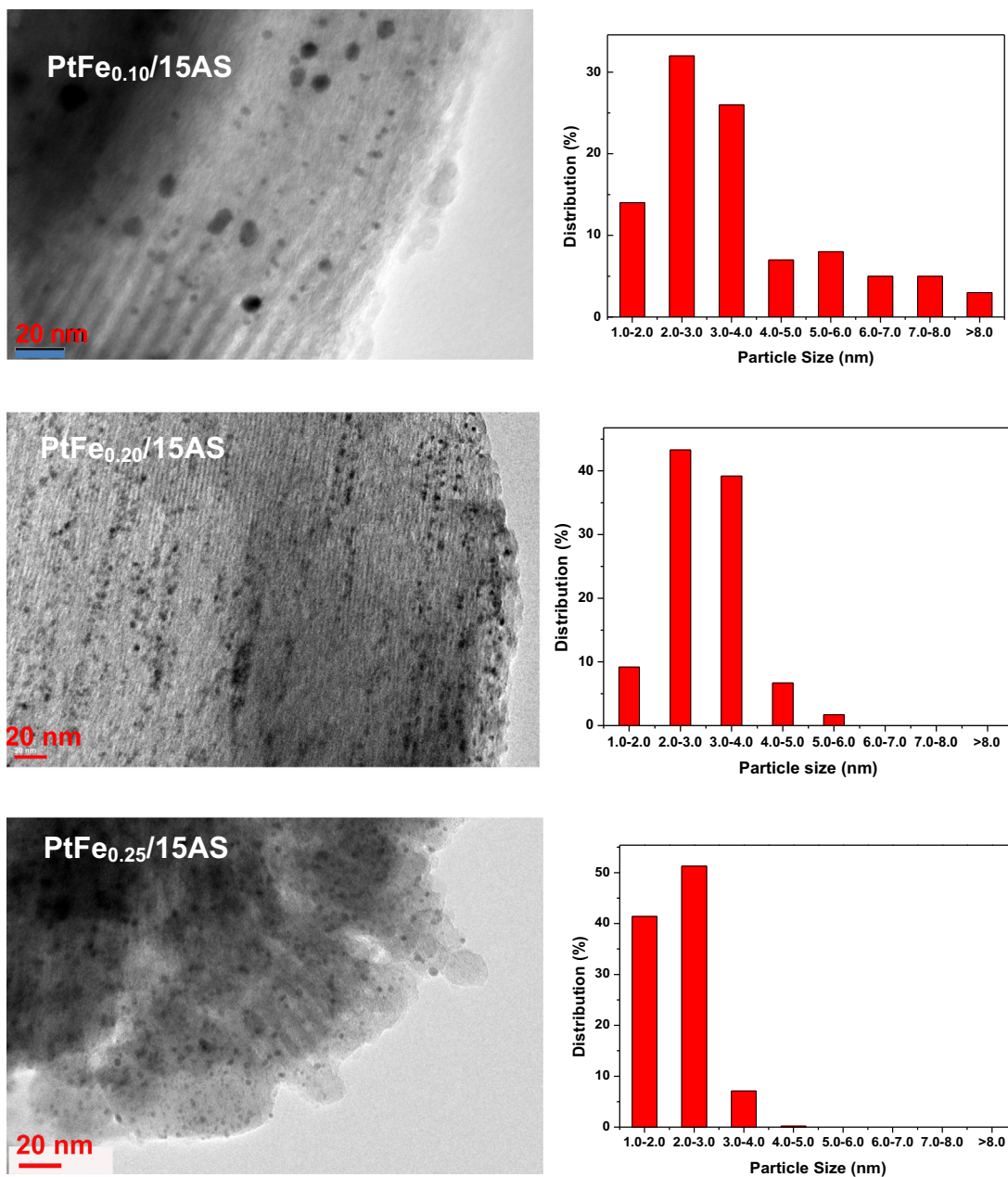


Fig. 8. TEM images and particle size distributions of PtFe<sub>x</sub>/15AS catalysts.

inferior activity (25.4% conversion of CAL) under the same conditions as those for the PtFe<sub>0.25</sub>/15AS catalyst, although the selectivity to COL of 90.9% is higher; thus the MSA<sub>COL</sub> (4.15 mol g<sub>Pt</sub><sup>-1</sup> h<sup>-1</sup>; see the red dot in the inset of Fig. 9) over this catalyst is much lower than that obtained with the PtFe<sub>0.25</sub>/15AS catalyst (10.71 mol g<sub>Pt</sub><sup>-1</sup> h<sup>-1</sup>). Moreover, a considerably decreased COL selectivity of 75.1% was afforded by the PtFe<sub>0.25</sub>/SBA-15 catalyst after the reaction time was prolonged (Entry 16, Table 2). Therefore, it could be concluded that not only FeO<sub>x</sub> but also Al<sub>2</sub>O<sub>3</sub>@-SBA-15 composite has significant influence on the catalytic behaviors.

Considering the different Pt particle sizes in the catalysts, TOF values based on surface Pt atoms for the PtFe<sub>x</sub>/15AS catalysts were also calculated and listed in Table 2. The addition of a low content of FeO<sub>x</sub> (Fe/Pt ≤ 0.25) greatly enhances the intrinsic activity of the catalysts. Hence, the PtFe<sub>0.25</sub>/15AS catalyst affords a TOF of 1.54 s<sup>-1</sup>, which is five times higher than that on the Pt/15AS catalyst. Since

the catalysts containing large amounts of FeO<sub>x</sub> (Fe/Pt > 0.25), such as PtFe<sub>0.3</sub>/15AS catalyst, usually have much larger Pt particles with much lower dispersion, and perfect Pt single crystals are also formed on the support surface (see the TEM image in Fig. S4), it is not reasonable to compare the TOF value of a Pt nanoparticle catalyst with that of a single-crystal catalyst. Therefore, the TOF values on these catalysts (Fe/Pt > 0.25) are not provided.

To fully understand the PtFe<sub>x</sub>/15AS catalysts, a comparison was also made between the TOF values obtained with Pt-Fe catalysts supported on different materials reported in the literature. For instance, the bimetallic Pt-Fe catalyst supported on mesoporous carbon prepared by the incipient wetness impregnation method afforded 0.049 s<sup>-1</sup> TOF, which was calculated according to the results obtained with PtFe/C-SA catalyst with a dispersion of 25% [39]. The Fe-doped Pt catalysts supported on zeolite P showed higher TOF values (20.7–80.7 × 10<sup>-2</sup> s<sup>-1</sup>) compared with the monometallic Pt catalyst (0.18–0.23 × 10<sup>-2</sup> s<sup>-1</sup>) [46]. Nevertheless,

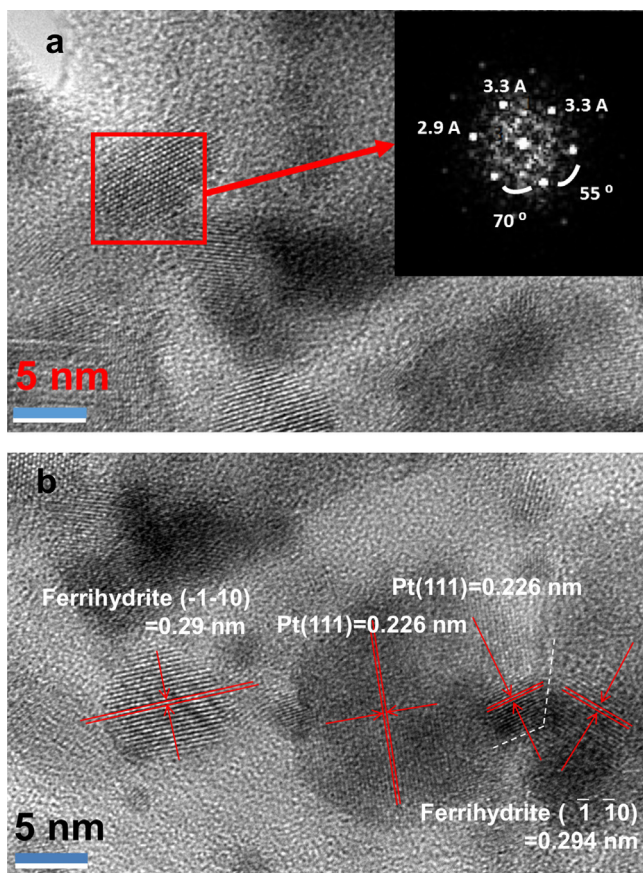


Fig. 9. HRTEM images of (a, b) PtFe<sub>0.25</sub>/15AS catalyst.

they are much lower than those obtained with PtFe<sub>x</sub>/15AS catalysts in this study. The bimetallic Pt–Fe catalyst supported on carbon nanotubes prepared by a two-step microwave heating method showed TOF 0.94–2.21 s<sup>-1</sup> for the liquid-phase hydrogenation of CAL under similar conditions [38], which are of the same magnitude as those obtained in our case. Additionally, although the authors did not report the TOF value for the very similar Pt–FeO<sub>x</sub>/SiO<sub>2</sub> catalysts prepared by a galvanic displacement method, the PtFe<sub>x</sub>/15AS catalysts in this study furnish higher MSA<sub>CAL</sub> and MSA<sub>COL</sub> than the Pt–FeO<sub>x</sub>/SiO<sub>2</sub> catalysts [47], which have been discussed above.

Furthermore, we also compared the results in this case with those obtained under similar conditions in the literature. As reported in Ref. [21], 5% Pt/CeO<sub>2</sub>–ZrO<sub>2</sub> catalyst showed TOF 1849 h<sup>-1</sup> (0.51 s<sup>-1</sup>) and 71.1% selectivity to COL at 100 °C under 20 bar hydrogen pressure. Another example is that 0.1 g of 5.4 wt % Co–1.7 wt % Pt/SiO<sub>2</sub> catalyst gave a 28.6% conversion of 3 ml CAL within 2 h, furnishing a selectivity to COL of 78% at 80 °C under a hydrogen pressure of 4.0 MPa [37]. Additionally, as discussed above, 50 mg of 0.8Pt–3.8FeO<sub>x</sub>/SiO<sub>2</sub> catalyst showed a 21% conversion of 0.5 ml CAL within 1 h, affording 84% selectivity to COL with a MSA<sub>CAL</sub> of 2.24 mol g<sub>Pt</sub><sup>-1</sup> h<sup>-1</sup> at 150 °C under a hydrogen pressure of 1.0 MPa [47]. In this study, 50 mg of PtFe<sub>0.25</sub>/15AS catalyst showed a 77.4% conversion of 22.5 mmol CAL (about 2.9 ml) within 0.5 h at 90 °C under a hydrogen pressure of 2.0 MPa, affording selectivity to COL of 76.9% with a TOF of 1.54 s<sup>-1</sup> and MSA<sub>CAL</sub> of 13.93 mol g<sub>Pt</sub><sup>-1</sup> h<sup>-1</sup>. Among the results mentioned above, the selectivity to COL is comparable. Nevertheless, the activity obtained in this study in terms of TOF or MSA<sub>CAL</sub> is the highest under similar reaction conditions.

Moreover, we also performed the selective hydrogenation of CAL with the PtFe<sub>0.25</sub>/15AS catalyst under milder conditions, such

as under lower hydrogen pressure or at ambient temperature. As listed in entry 8 of Table 1, the reaction performed at ambient temperature also afforded medium CAL conversion and good COL selectivity. Accordingly, a TOF of 0.44 s<sup>-1</sup> was furnished by the PtFe<sub>0.25</sub>/15AS catalyst at room temperature, which is comparable to those reported in the literature as obtained at higher temperatures [46], but much higher than those reported in Ref. [39]. As for the MSA<sub>COL</sub> obtained with the PtFe<sub>0.25</sub>/15AS catalyst at room temperature, it is nearly twice that reported in Ref. [47]. Additionally, the similar reaction results obtained under lower hydrogen pressure, such as 1.0 MPa and 1 bar, confirm that the selective hydrogenation of CAL is a zero-order reaction with regard to hydrogen pressure.

#### 3.4. Further characterization of PtFe<sub>x</sub>/15AS catalysts

To deeply understand the superior ability of the PtFe<sub>x</sub>/15AS catalyst, especially the PtFe<sub>0.25</sub>/15AS catalyst, the relevant catalysts were further characterized using a series of techniques. First, a close investigation of the morphology of the PtFe<sub>0.25</sub>/15AS catalyst was conducted using HRTEM (Fig. 9). The presence of FeO<sub>x</sub> is confirmed by Fourier transformation (FT) identification (Fig. 9a), with the spots at 0.29 and 0.33 nm corresponding to the (2 0 2) and (−4 1 1) planes of ε-Fe<sub>2</sub>O<sub>3</sub>, respectively. Also, the lattice fringe of 0.226 nm is assigned to the Pt(1 1 1) plane, as shown in Fig. 9b. In addition to the isolated ε-Fe<sub>2</sub>O<sub>3</sub> entities, some ε-Fe<sub>2</sub>O<sub>3</sub> particles are contacting Pt particles (indicated by the white line), suggesting interactions between Pt and ε-Fe<sub>2</sub>O<sub>3</sub>.

To further characterize the distribution of Pt and FeO<sub>x</sub> in the PtFe<sub>x</sub>/15AS catalysts, the HAADF-STEM images for some catalysts were taken. As shown in Fig. 10, for both PtFe<sub>0.10</sub>/15AS and PtFe<sub>0.25</sub>/15AS catalysts, the Pt atoms form aggregations, as evidenced by the bright spots in the STEM images; while the Fe atoms are uniformly distributed without forming any aggregation. Nevertheless, the signals of Pt are spatially associated with the Fe signals, suggesting that the Pt entities are closely related to the Fe element.

To study the electronic states of Pt and Fe, some representative catalysts were further characterized by DRIFTS using CO as a probe molecule. The IR spectroscopic study of CO adsorption is one of the methods commonly used to gain insight into electronic properties. To allow a direct comparison of these data with the catalytic results, the PtFe<sub>x</sub>/15AS catalysts were pretreated in a hydrogen flow at 400 °C for 2 h before IR spectra were taken. Fig. 11 shows the DRIFT spectra of CO adsorbed on PtFe<sub>x</sub>/15AS catalysts after purging with nitrogen at 35 °C for 1 h. For all the tested catalysts, only one mode of CO adsorption, linearly adsorbed CO, is identified. As displayed in Fig. 11, CO linearly adsorbed onto PtFe<sub>x</sub>/15AS catalysts shows a broad band centered at 2073–2081 cm<sup>-1</sup>. For instance, the PtFe<sub>0.10</sub>/15AS catalyst shows a linear CO adsorption at 2073 cm<sup>-1</sup> and the PtFe<sub>0.20</sub>/15AS catalyst gives a linearly adsorbed CO band centered at 2077 cm<sup>-1</sup>. As for the IR band of CO linearly adsorbed on PtFe<sub>0.25</sub>/15AS catalyst, it is centered at 2081 cm<sup>-1</sup>, a slightly higher CO vibration frequency than for the other two PtFe<sub>x</sub>/15AS catalysts. The CO band position in this case is a little higher than that observed on Pt catalysts supported on alumina or on silica [48]. This means that the electron density was somewhat lower on the PtFe<sub>x</sub>/15AS catalyst [48,49]. In other words, relatively strong interaction between Pt nanoparticles and Al<sub>2</sub>O<sub>3</sub>@SBA-15 composites or FeO<sub>x</sub> occurred during calcination in air at 500 °C. The charge transfer took place from Pt nanoparticles to the Lewis acids and Brønsted acids in the Al<sub>2</sub>O<sub>3</sub>@SBA-15 composites or to FeO<sub>x</sub> [42].

Considering that the three PtFe<sub>x</sub>/15AS catalysts characterized by CO-DRIFTS have similar Pt particle size distribution and that the average Pt particle size is in the range of 1.8–2.5 nm, the tiny influence of Pt particle size on the CO vibration band can be neglected.

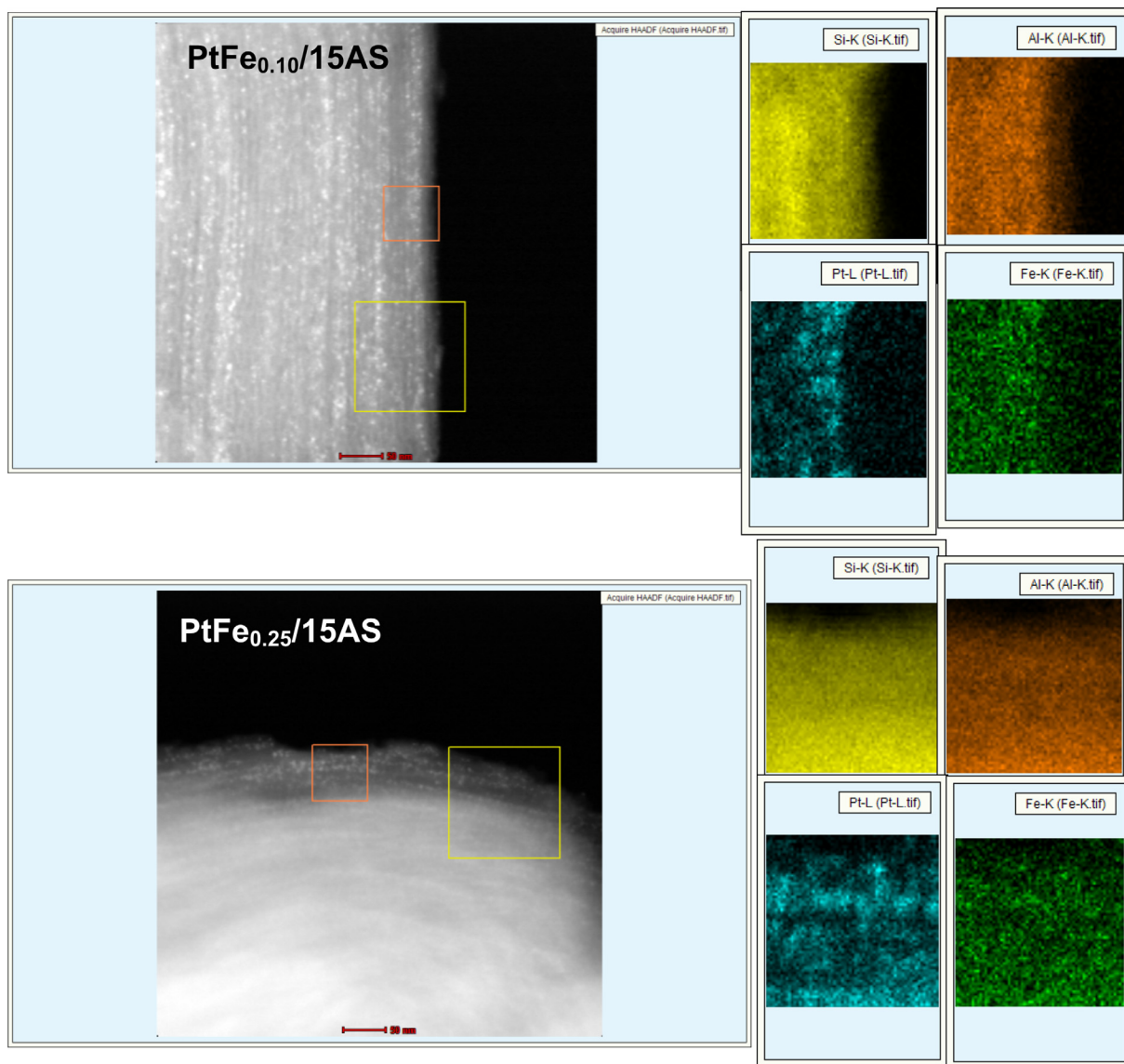


Fig. 10. HAADF-STEM images of  $\text{PtFe}_x/15\text{AS}$  catalysts and STEM-EDS elemental mapping images for the area enclosed by the orange square.

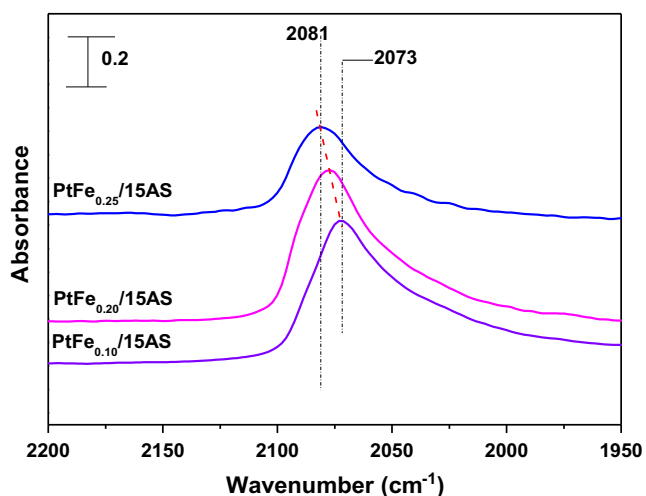


Fig. 11. DRIFTS spectra for CO adsorbed onto the  $\text{PtFe}_x/15\text{AS}$  catalysts after purging with  $\text{N}_2$  at 35 °C for 1 h.

Thus, the lower CO vibration position reflects that the catalyst has higher electron density on Pt, because an increase in the electron density on Pt in turn increases the extent of back donation to the  $\text{CO } 2\pi^*$  orbitals. The increase in the electron density on Pt might be contributed by electron transfer from  $\text{FeO}_x$  to Pt nanoparticles. This phenomenon is quite common for Fe-related bimetallic systems [50]. Based on the above discussion, the  $\text{PtFe}_{0.25}/15\text{AS}$  catalyst has the lowest electron density on Pt among the three  $\text{PtFe}_x/15\text{AS}$  catalysts characterized by CO-DRIFTS. This indicates that the Pt– $\text{FeO}_x$  interaction in the  $\text{PtFe}_x/15\text{AS}$  catalysts is quite different with different Fe amounts. As already mentioned above, there is electron transfer from  $\text{FeO}_x$  to Pt atoms for  $\text{PtFe}_{0.10}/15\text{AS}$  and  $\text{PtFe}_{0.20}/15\text{AS}$  catalysts. However, because the  $\text{PtFe}_{0.25}/15\text{AS}$  catalyst is more electron-deficient than the  $\text{PtFe}_{0.10}/15\text{AS}$  and  $\text{PtFe}_{0.20}/15\text{AS}$  catalysts, electron transfer might occur in the  $\text{PtFe}_{0.25}/15\text{AS}$  catalyst from Pt to  $\text{FeO}_x$  instead [47].

The Pt– $\text{Al}_2\text{O}_3/\text{SBA-15}$  interaction and Pt– $\text{FeO}_x$  interaction were further confirmed by the  $\text{H}_2$  TPR results, as shown in Fig. 12. For the monometallic Pt/15AS catalyst, there are two reduction peaks, one centered at 94 °C and the other at 345 °C. The low-temperature reduction peak is assigned to the reduction of either  $\text{PtO}_2$  or bulk

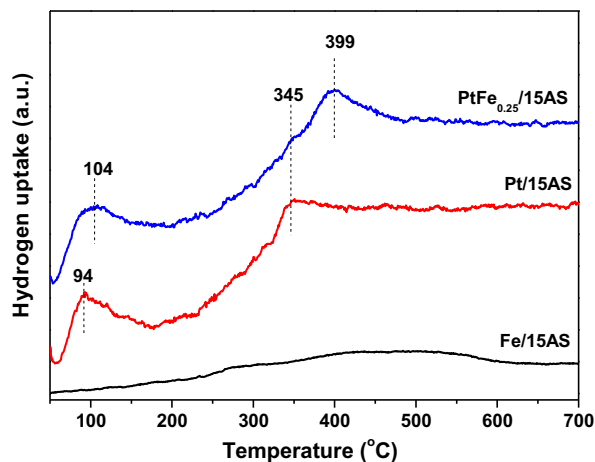


Fig. 12.  $\text{H}_2$  TPR profiles of as-prepared (calcined) 0.36 wt% Fe/15AS, 5 wt% Pt/15AS, and  $\text{PtFe}_{0.25}/15\text{AS}$  (5 wt% Pt–0.36 wt% Fe) catalysts.

$\text{PtO}_x$  species interacting with the oxygen atoms of the support. The second peak can be attributed to highly dispersed particles with strong interaction with the support [51]. The existence of these species may be related to the ability of  $\text{Al}_2\text{O}_3/\text{SBA-15}$  to stabilize oxidized Pt particles on its surface. For the bimetallic  $\text{PtFe}_{0.25}/15\text{AS}$  catalyst, the reduction needs a slightly higher temperature. The peak centered at lower temperature shifted to 104 °C and the one centered at higher temperature shifted to 399 °C, about 44 °C higher than that for the monometallic Pt/15AS catalyst. This indicates that the intimate and strong Pt– $\text{FeO}_x$  interaction occurs in the  $\text{PtFe}_{0.25}/15\text{AS}$  catalyst, in good agreement with the HRTEM and HAADF-STEM results. For reference, a Fe/15AS sample with the same Fe loading of 0.36 wt% as that for the  $\text{PtFe}_{0.25}/15\text{AS}$  catalyst was also prepared and characterized using  $\text{H}_2$  TPR. The reduction of  $\text{FeO}_x$  occurred at relatively higher temperature and showed a very broad but weak peak in the range of 400–600 °C [52]. Accordingly, we also calculated the  $\text{H}_2$  consumption of each catalyst as follows:  $\text{H}_2$  uptake for the 0.36 wt% Fe/15AS, 5 wt% Pt/15AS, and  $\text{PtFe}_{0.25}/15\text{AS}$  containing 5 wt% Pt and 0.36 wt% Fe was 0.025, 0.31, and 0.35  $\text{mmol g}^{-1}$ , respectively. The  $\text{H}_2/\text{Pt}$  and  $\text{H}_2/\text{Fe}$  ratios were also calculated accordingly. As a result, the  $\text{H}_2/\text{Pt}$  ratio was about 1.2, lower than the stoichiometric value of 2.0 if chloroplatinic acid was completely reduced to  $\text{Pt}^0$  species. This suggests that Pt species cannot be fully reduced before the reaction starts, mainly due to strong interaction of Pt species with 15AS and  $\text{FeO}_x$  species. With regard to the  $\text{H}_2/\text{Fe}$  ratio, it is only 0.4 even if the reduction is continued till 700 °C during the  $\text{H}_2$  TPR experiments, much lower than the stoichiometric value of 1.5 if  $\text{Fe}^{3+}$  were fully reduced to  $\text{Fe}^0$ . On recalling that the catalyst precursor was reduced at 500 °C and pretreated at 400 °C in flowing hydrogen before being submitted to the hydrogenation reaction, we can conclude that Fe species are in the oxidation state to a great extent.

The oxidation states of the elements in the  $\text{PtFe}_{0.25}/15\text{AS}$  catalyst probed with XPS after in situ pretreatment in a hydrogen flow at 400 °C for 2 h are shown in Fig. 13. It can be observed that there is an overlap between Pt 4f and Al 2p peak at about 70.0–79.0 eV (Fig. 13a). However, the peaks can be easily deconvoluted to Al 2p and Pt 4f regions. The BE at 71.3 eV in the Pt 4f region can be assigned to  $4f_{7/2}$  of the  $\text{Pt}^0$  species. The BE at 72.3 eV is lower than that for  $\text{Pt}4f_{7/2}$  of the  $\text{Pt}^{2+}$  species, but higher than that for  $\text{Pt}4f_{7/2}$  of the  $\text{Pt}^0$  species; therefore, it can be attributed to  $\text{Pt}4f_{7/2}$  of partially charged  $\text{Pt}^{\delta+}$  species ( $0 < \delta < 2$ ). Since the BEs of Al 2p and Pt 4f are overlapped, the Pt 4d spectrum was taken as well. The Pt 4d spectrum clearly shows two components at binding energies of 314.2 and 315.9 eV (Fig. 13b). The former is assigned to metallic  $\text{Pt}^0$  [53], and the latter could be assigned to positively charged  $\text{Pt}^{\delta+}$

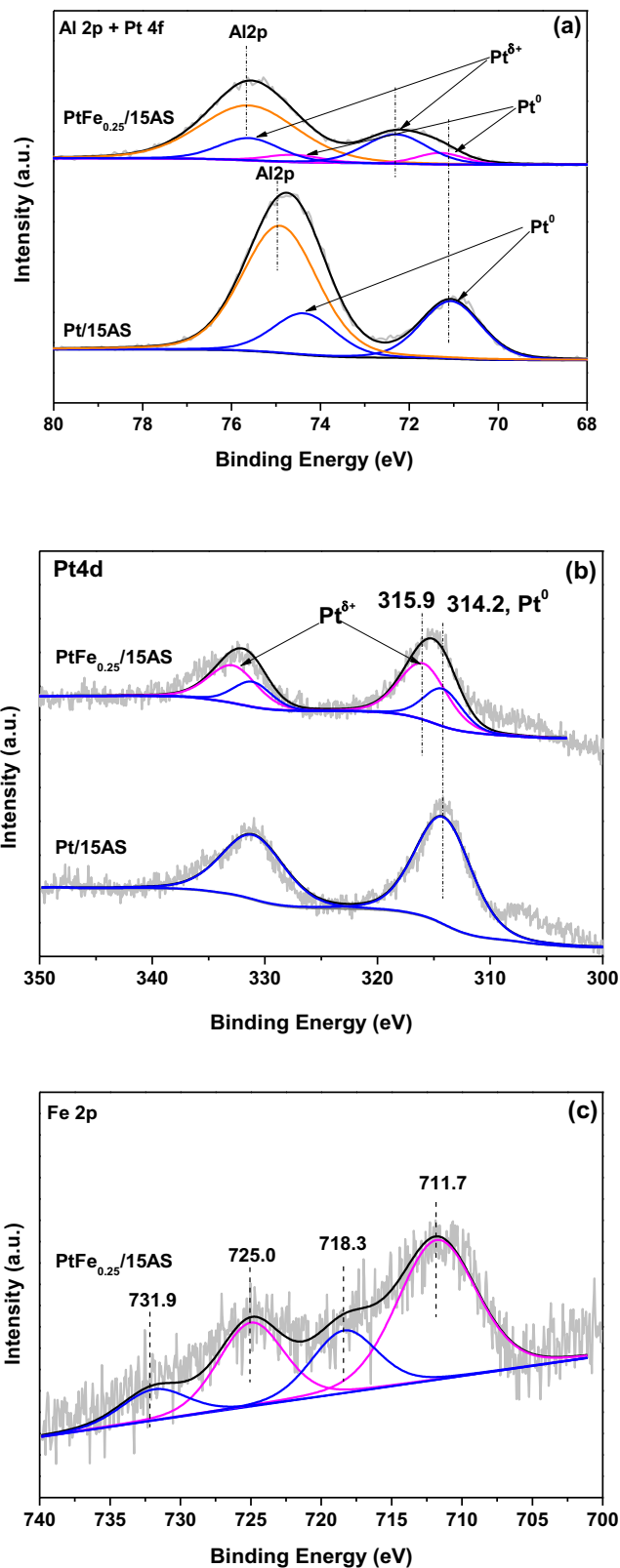


Fig. 13. XPS spectra of (a) Al 2p + Pt 4f, (b) Pt 4d for  $\text{PtFe}_{0.25}/15\text{AS}$  and Pt/15AS catalysts, and (c) Fe 2p for  $\text{PtFe}_{0.25}/15\text{AS}$  catalyst.

species ( $0 < \delta < 2$ ), because its BE is lower than that of typical  $\text{Pt}^{2+}$  (316.3 eV) [54].

Moreover, the  $\text{Pt}^{\delta+}$  species are dominant on the catalyst surface. With regard to the origin of the  $\text{Pt}^{\delta+}$  species, they could result from

the strong interaction of Pt nanoparticles with  $\text{Al}_2\text{O}_3@\text{SBA-15}$  and electron transfer from Pt atoms to  $\text{Al}_2\text{O}_3@\text{SBA-15}$  during the calcination process at 500 °C in air before reduction. Additionally, electron transfer from Pt atoms to  $\text{FeO}_x$  occurs in the  $\text{PtFe}_{0.25}/15\text{AS}$  catalyst, which has already been identified by the CO-DRIFTS results. For comparison, the Pt/15AS catalyst was also characterized by XPS. As displayed in Fig. 13, the deconvoluted XP spectrum of the Pt/15AS catalyst only showed one Pt species ( $\text{Pt}^0$ ). This implies that the interaction between Pt and  $\text{FeO}_x$  is very strong for the  $\text{PtFe}_{0.25}/15\text{AS}$  catalyst. Of particular note is that the signal intensity for  $\text{PtFe}_{0.25}/15\text{AS}$  is weaker than that for the Pt/15AS, maybe due to Fe species covering the Pt surface [39].

The  $\text{Fe}2p$  XPS spectra of samples are shown in Fig. 13c. Iron species are too complicated to assign from the deconvolution curves, especially for BE above 715.0 eV. Due to BE of  $2p_{3/2}$  for  $\text{FeO}$ ,  $\text{Fe}_3\text{O}_4$ , and  $\text{Fe}_2\text{O}_3$  overlapping at around 711.0 eV [55], we cannot identify them as one specific species just from the XPS results. Nevertheless, from the  $\text{H}_2$  TPR profile of  $\text{PtFe}_{0.25}/15\text{AS}$ , the Fe species are reduced at 400–600 °C, while the catalyst precursor is reduced at 500 °C in this case. Furthermore, in combination with the HRTEM image of the  $\text{PtFe}_{0.25}/15\text{AS}$  catalyst, we can deduce that Fe species are  $\varepsilon\text{-Fe}_2\text{O}_3$ .

The above results reflect a strong interaction between Pt and  $\text{Al}_2\text{O}_3@\text{SBA-15}$  and between Pt and  $\text{FeO}_x$ . This interaction changes the electronic properties of Pt nanoparticles, which can certainly explain the enhanced performance of  $\text{PtFe}_{0.25}/15\text{AS}$  catalysts in the selective hydrogenation of CAL. The predominant Pt species in the  $\text{PtFe}_{0.25}/15\text{AS}$  catalyst are electron-deficient  $\text{Pt}^{\delta+}$  species, and iron species are also in oxidation states. Electron transfer from Pt to  $\text{Al}_2\text{O}_3@\text{SBA-15}$  and from Pt to  $\text{FeO}_x$  causes electron-deficient Pt species in the  $\text{PtFe}_{0.25}/15\text{AS}$  catalyst.

In our opinion, the electron-deficient state of Pt particles ( $\text{Pt}^{\delta+}$ ) is beneficial for adsorption and activation of carbonyl bonds via interaction of oxygen atoms in carbonyl groups with  $\text{Pt}^{\delta+}$  species [56]. Furthermore, the  $\text{FeO}_x$  species are also helpful for adsorption of terminal carbonyl bonds. Meanwhile, hydrogen atoms can attack the activated carbonyl group of CAL via dissociative adsorption onto  $\text{Pt}^0$  species to form the desired product, COL. Hence, the

$\text{PtFe}_{0.25}/15\text{AS}$  catalyst with Pt nanoparticles containing predominant  $\text{Pt}^{\delta+}$  species furnishes the best catalytic performance in terms of CAL conversion and COL selectivity. According to the discussion, the related hypothesis of CAL adsorption and activation with the  $\text{PtFe}_x/15\text{AS}$  catalyst was also proposed (Fig. 14). Both the positive  $\text{Pt}^{\delta+}$  species and the  $\text{FeO}_x$  species can adsorb and activate CAL by interaction with oxygen atoms in carbonyl groups, while hydrogen molecules are dissociated on  $\text{Pt}^0$  atoms and the then transferred to attack the activated CAL to form COL.

#### 4. Conclusions

Mesoporous  $\text{Al}_2\text{O}_3@\text{SBA-15}$  composites (15AS)-supported monometallic Pt or bimetallic Pt–Fe catalysts were applied for the liquid-phase selective hydrogenation of CAL. As a result, Fe-doped  $\text{PtFe}_x/15\text{AS}$  catalysts are proved to be active and selective for hydrogenation of CAL to the unsaturated alcohol COL, even under milder conditions such as at room temperature or under atmospheric hydrogen pressure. The reaction rate of the  $\text{PtFe}_x/15\text{AS}$  catalyst varies with the Fe amount, and a volcano-like curve between the reaction rate and the Fe/Pt molar fraction is observed. When the Fe/Pt molar ratio is 0.25, the  $\text{PtFe}_{0.25}/15\text{AS}$  catalyst reaches a maximum mass-specific rate of  $13.93 \text{ mol}_{\text{CAL}} \text{ g}_{\text{Pt}}^{-1} \text{ h}^{-1}$ , with a selectivity to COL of 76.9%. According to the corresponding characterizations of  $\text{PtFe}_x/15\text{AS}$  catalysts, the Pt particles with positive charges, that is, with  $\text{Pt}^{\delta+}$  species as dominant species on the catalyst surface, are derived from electron transfer from Pt atoms to  $\text{Al}_2\text{O}_3@\text{SBA-15}$  and from Pt to  $\text{FeO}_x$ . In addition, the Fe species also in oxidation states are in close vicinity to the Pt species. Therefore, the Pt species with positive charges are beneficial for the preferential adsorption and activation of terminal C=O groups. Furthermore, the  $\text{FeO}_x$  species are also helpful for adsorption of terminal carbonyl bonds. Meanwhile, hydrogen atoms can attack the activated carbonyl group of CAL via dissociative adsorption onto  $\text{Pt}^0$  species to form the desired product COL. Hence, the activity and selectivity to the unsaturated alcohol are both greatly enhanced with the  $\text{PtFe}_{0.25}/15\text{AS}$  catalyst.

#### Acknowledgments

This work was supported by the National Natural Science Foundation of China (Grants 21273076 and 21373089), the Open Research Fund of the Top Key Discipline of Chemistry in Zhejiang Provincial Colleges and the Key Laboratory of the Ministry of Education for Catalysis Materials (Zhejiang Normal University) (ZJHX2013), and a Shanghai Leading Academic Discipline Project (B409). W. Xie also acknowledges the sponsorship of the Natural Science Foundation of Shanghai (Grant 15ZR1411400).

#### References

- [1] G. Neri, L. Bonaccorsi, L. Mercadante, S. Galvagno, Kinetic analysis of cinnamaldehyde hydrogenation over aluminum-supported ruthenium catalyst, *Ind. Eng. Chem. Res.* 36 (1997) 3554–3562.
- [2] R. Nie, M. Miao, W. Du, J. Shi, Y. Liu, Z. Hou, Selective hydrogenation of C=C bond over N-doped reduced graphene oxides supported Pd catalyst, *Appl. Catal. B* 180 (2016) 607–613.
- [3] V. Ponec, On the role of promoters in hydrogenations on metals;  $\alpha,\beta$ -unsaturated aldehydes and ketones, *Appl. Catal. A* 149 (1997) 27–48.
- [4] B. Coq, F. Figueras, Structure-activity relationships in catalysis by metals: some aspects of particle size, bimetallic and supports effects, *Coord. Chem. Rev.* 178–180 (1998) 1753–1783.
- [5] Y. Yuan, S. Yao, M. Wang, S. Lou, N. Yan, Recent Progress in chemoselective hydrogenation of  $\alpha, \beta$ -unsaturated aldehyde to unsaturated alcohol over nanomaterials, *Curr. Org. Chem.* 17 (2013) 400–413.
- [6] A. Giroir-Fendler, D. Richard, P. Gallezot, Selectivity in cinnamaldehyde hydrogenation of group-VIII metals supported on graphite and carbon, *Stud. Surf. Sci. Catal.* 41 (1988) 171–178.
- [7] P. Gallezot, D. Richard, Selective hydrogenation of  $\alpha, \beta$ -unsaturated aldehydes, *Catal. Rev. Sci. Eng.* 40 (1998) 81–126.

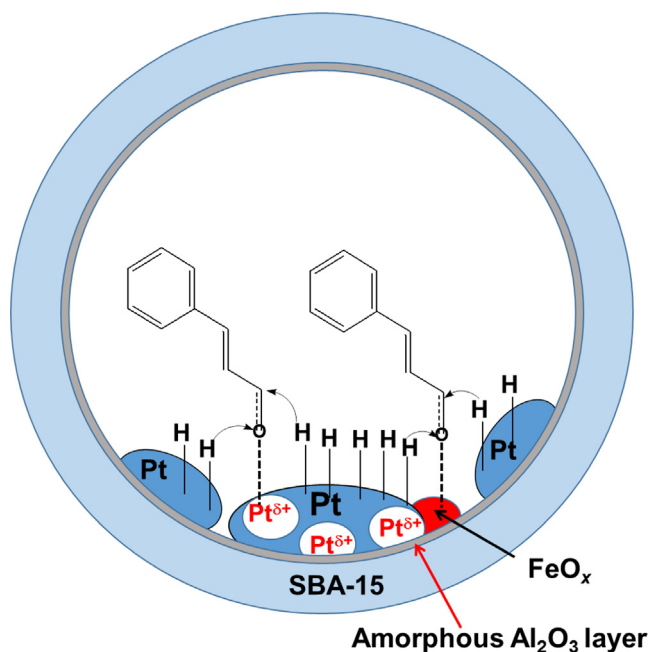


Fig. 14. The hypothesis of CAL adsorption and activation with the  $\text{PtFe}_x/15\text{AS}$  catalyst.

- [8] L.J. Durndell, C.M.A. Parlett, N.S. Hondow, M.A. Isaacs, K. Wilson, A.F. Lee, Selectivity control in Pt-catalyzed cinnamaldehyde hydrogenation, *Sci. Rep.* 5 (2015), srep09425.
- [9] W.O. Oduro, N. Cailuo, K.M. Yu, H. Yang, S.C. Tsang, Geometric and electronic effects on hydrogenation of cinnamaldehyde over unsupported Pt-based nanocrystals, *Phys. Chem. Chem. Phys.* 13 (2011) 2590–2602.
- [10] A.J. Plomp, H. Vuori, A.O.I. Krause, K.P. de Jong, J.H. Bitter, Particle size effects for carbon nanofiber supported platinum and ruthenium catalysts for the selective hydrogenation of cinnamaldehyde, *Appl. Catal. A* 351 (2008) 9–15.
- [11] A.K. Prashar, S. Mayadevi, R. Nandini, Devi, Effect of particle size on selective hydrogenation of cinnamaldehyde by Pt encapsulated in mesoporous silica, *Catal. Commun.* 28 (2012) 42–46.
- [12] A. Giroir-Fendler, D. Richard, P. Gallezot, Chemoselectivity in the catalytic hydrogenation of cinnamaldehyde: effect of metal particle morphology, *Catal. Lett.* 5 (1990) 175–182.
- [13] S.C. Tsang, N. Cailuo, B. Thiebaut, W. Oduro, J. Cookson, A.T.S. Kong, P. Bishop, Engineering preformed cobalt-doped platinum nanocatalysts for ultraselective hydrogenation, *ACS Nano* 2 (2008) 2547–2553.
- [14] P. Gallezot, A. Giroir-Fendler, D. Richard, Chemoselectivity in cinnamaldehyde hydrogenation induced by shape selectivity effects in Pt-Y zeolite catalysts, *Catal. Lett.* 5 (1990) 169–174.
- [15] G. Guo, F. Qin, D. Yang, C. Wang, H. Xu, S. Yang, Synthesis of platinum nanoparticles supported on poly(acrylic acid) grafted MWNTs and their hydrogenation of citral, *Chem. Mater.* 20 (2008) 2291–2297.
- [16] Y. Zhu, F. Zaera, Selectivity in the catalytic hydrogenation of cinnamaldehyde promoted by Pt/SiO<sub>2</sub> as a function of metal nanoparticle size, *Catal. Sci. Technol.* 4 (2014) 955–962.
- [17] J. Shi, R. Nie, P. Chen, Z. Hou, Selective hydrogenation of cinnamaldehyde over reduced graphene oxide supported Pt catalyst, *Catal. Commun.* 41 (2013) 101–105.
- [18] A.B. Boffa, C. Lin, A.T. Bell, G.A. Somorjai, Lewis acidity as an explanation for oxide promotion of metals: implications of its importance and limits for catalytic reactions, *Catal. Lett.* 27 (1994) 243–249.
- [19] M. Englisch, A. Jentys, J.A. Lercher, Structure sensitivity of the hydrogenation of crotonaldehyde over Pt/SiO<sub>2</sub> and Pt/TiO<sub>2</sub>, *J. Catal.* 166 (1997) 25–35.
- [20] S. Handjani, E. Marceau, J. Blanchard, J.-M. Krafft, M. Che, P. Mäki-Arvela, N. Kumar, J. Wärnä, D.Y. Murzin, Influence of the support composition and acidity on the catalytic properties of mesoporous SBA-15, Al-SBA-15, and Al<sub>2</sub>O<sub>3</sub>-supported Pt catalysts for cinnamaldehyde hydrogenation, *J. Catal.* 282 (2011) 228–236.
- [21] S. Bhogswararao, D. Srinivas, Intramolecular selective hydrogenation of cinnamaldehyde over CeO<sub>2</sub>-ZrO<sub>2</sub>-supported Pt catalysts, *J. Catal.* 285 (2012) 31–40.
- [22] B.F. Machado, S. Morales-Torres, A.F. Pérez-Cadenas, F.J. Maldonado-Hódar, F. Carrasco-Marín, A.M.T. Silva, J.L. Figueiredo, J.L. Faria, Preparation of carbon aerogel supported platinum catalysts for the selective hydrogenation of cinnamaldehyde, *Appl. Catal. A* 425–426 (2012) 161–169.
- [23] P.V. Samant, M.F.R. Pereira, J.L. Figueiredo, Mesoporous carbon supported Pt and Pt-Sn catalysts for hydrogenation of cinnamaldehyde, *Catal. Today* 102–103 (2005) 183–188.
- [24] X. Ji, X. Niu, B. Li, Q. Han, F. Yuan, F. Zaera, Y. Zhu, H. Fu, Selective hydrogenation of cinnamaldehyde to cinnamal alcohol over platinum/graphene catalysts, *ChemCatChem* 6 (2014) 3246–3253.
- [25] Z. Guo, C. Xiao, R.V. Maliga-Ganesh, L. Zhou, T.W. Goh, X. Li, D. Tesfagaber, A. Thiel, W. Huang, Pt nanoclusters confined within metal-organic framework cavities for chemoselective cinnamaldehyde hydrogenation, *ACS Catal.* 4 (2014) 1340–1348.
- [26] K.B. Vu, K.V. Bukhryakov, D.H. Anjum, V.O. Rodionov, Surface-bound ligands modulate chemoselectivity and activity of a bimetallic nanoparticle catalyst, *ACS Catal.* 5 (2015) 2529–2533.
- [27] B. Wu, H. Huang, J. Yang, N. Zheng, G. Fu, Selective hydrogenation of  $\alpha,\beta$ -unsaturated aldehydes catalyzed by amine-capped platinum-cobalt nanocrystals, *Angew. Chem. Int. Ed.* 51 (2012) 3440–3443.
- [28] K.R. Kahsar, D.K. Schwartz, J.W. Medlin, Control of metal catalyst selectivity through specific noncovalent molecular interactions, *J. Am. Chem. Soc.* 136 (2014) 520–526.
- [29] K.R. Kahsar, D.K. Schwartz, J.W. Medlin, Stability of self-assembled monolayer coated Pt/Al<sub>2</sub>O<sub>3</sub> catalysts for liquid phase hydrogenation, *J. Mol. Catal. A* 396 (2015) 188–195.
- [30] M. Bidaoui, C. Especel, S. Sabour, L. Benatallah, N. Saib-Bouchenafa, S. Royer, O. Mohammedi, Toward the improvement in unsaturated alcohol selectivity during  $\alpha,\beta$ -unsaturated aldehyde selective hydrogenation, using Zn as promoter of Pt, *J. Mol. Catal. A* 399 (2015) 97–105.
- [31] T. Li, G. Li, Y. Xu, The modification effect of Sn on Pt/Al<sub>2</sub>O<sub>3</sub> catalyst for selective hydrogenation of cinnamaldehyde, *Chin. J. Catal.* 20 (1999) 219–223.
- [32] T. Ekou, A. Vicente, G. Lafaye, C. Especel, P. Marecot, Bimetallic Rh-Ge and Pt-Ge catalysts supported on TiO<sub>2</sub> for citral hydrogenation: II. Catalytic properties, *Appl. Catal. A* 314 (2006) 73–80.
- [33] P.-F. Qu, J.-G. Chen, Y.-H. Song, Z.-T. Liu, Z.-W. Liu, Y. Li, J. Lu, J. Jiang, Effect of Fe (III) on hydrogenation of citral over Pt supported multiwalled carbon nanotube, *Catal. Commun.* 68 (2015) 105–109.
- [34] J.P. Stassi, P.D. Zgolicz, S.R. de Miguel, O.A. Scelza, Formation of different promoted metallic phases in PtFe and PtSn catalysts supported on carbonaceous materials used for selective hydrogenation, *J. Catal.* 306 (2013) 11–29.
- [35] K. Taniya, T. Hara, T. Imai, Y. Ichihashi, S. Nishiyama, Preparation of Silica-coated SnPt bimetallic nanoparticle catalysts for the selective hydrogenation of cinnamaldehyde, *J. Chem. Eng. Jpn.* 47 (2014) 130–135.
- [36] Z. Rong, Z. Sun, Y. Wang, J. Lv, Y. Wang, Selective hydrogenation of cinnamaldehyde to cinnamyl alcohol over graphene supported Pt-Co bimetallic catalysts, *Catal. Lett.* 144 (2014) 980–986.
- [37] R. Zheng, M.D. Porosoff, J.L. Weiner, S. Lu, Y. Zhu, J.G. Chen, Controlling hydrogenation of C=O and C=C bonds in cinnamaldehyde using silica supported Co-Pt and Cu-Pt bimetallic catalysts, *Appl. Catal. A* 419–420 (2012) 126–132.
- [38] Z. Guo, C. Zhou, D. Shi, Y. Wang, X. Jia, J. Chang, A. Borgna, C. Wang, Y. Yang, Toward the decoration of Pt nanoparticles supported on carbon nanotubes with Fe oxides and its effect on the catalytic reaction, *Appl. Catal. A* 435–436 (2012) 131–140.
- [39] N. Mahata, F. Gonçalves, M.F.R. Pereira, J.L. Figueiredo, Selective hydrogenation of cinnamaldehyde to cinnamyl alcohol over mesoporous carbon supported Fe and Zn promoted Pt catalyst, *Appl. Catal. A* 339 (2008) 159–168.
- [40] Q. Zheng, D. Wang, F. Yuan, Q. Han, Y. Dong, Y. Liu, X. Niu, Y. Zhu, An effective Co-promoted platinum of Co-Pt/SBA-15 catalyst for selective hydrogenation of cinnamaldehyde to cinnamyl Alcohol, *Catal. Lett.* 146 (2016) 1535–1543.
- [41] Z. Liu, X. Tan, J. Li, C. Lv, Easy synthesis of bimetal PtFe-containing ordered mesoporous carbons and their use as catalysts for selective cinnamaldehyde hydrogenation, *New J. Chem.* 37 (2013) 1350–1357.
- [42] X. Li, H. Wang, H. Pan, Y.M. Wang, P. Wu, Pt nanoparticles entrapped in Al<sub>2</sub>O<sub>3</sub>@SBA-15 composites: effective and recyclable catalysts for enantioselective hydrogenation of ethyl 2-oxo-4-phenylbutyrate, *Appl. Catal. A* 488 (2014) 48–57.
- [43] H. Wang, X. Li, Y.M. Wang, P. Wu, Pt nanoparticles supported on highly dispersed alumina coated inside SBA-15 for enantioselective hydrogenation, *ChemCatChem* 2 (2010) 1303–1311.
- [44] D. Zhao, J. Feng, Q. Huo, N. Melosh, G.H. Fredrickson, B.F. Chmelka, G.D. Stucky, Triblock copolymer synthesis of mesoporous silica with periodic 50 to 300 angstrom pores, *Science* 279 (1998) 548–552.
- [45] S.T. Oyama, X. Zhang, J. Lu, Y. Gu, T. Fujitani, Epoxidation of propylene with H<sub>2</sub> and O<sub>2</sub> in the explosive regime in a packed-bed catalytic membrane reactor, *J. Catal.* 257 (2008) 1–4.
- [46] G. Neri, I. Arrigo, F. Corigliano, L. De Luca, A. Donato, Selective hydrogenation of cinnamaldehyde on Pt and Pt-Fe catalysts supported on zeolite P, *Catal. Lett.* 141 (2011) 1590–1597.
- [47] Y. Shi, Zi. Yuan, Q. Wei, K. Sun, B. Xu, Pt-FeO<sub>x</sub>/SiO<sub>2</sub> catalysts prepared by galvanic displacement show high selectivity for cinnamyl alcohol production in the chemoselective hydrogenation of cinnamaldehyde, *Catal. Sci. Technol.* 6 (2016) 7033–7037.
- [48] X. Li, X. You, P. Ying, J. Xiao, C. Li, Some insights into the preparation of Pt/ $\gamma$ -Al<sub>2</sub>O<sub>3</sub> catalysts for the enantioselective hydrogenation of  $\alpha$ -ketoesters, *Top. Catal.* 25 (2003) 63–70.
- [49] X. Li, W. Zheng, H. Pan, Y. Yu, L. Chen, P. Wu, Pt nanoparticles supported on highly dispersed TiO<sub>2</sub> coated on SBA-15 as an efficient and recyclable catalyst for liquid-phase hydrogenation, *J. Catal.* 300 (2013) 9–19.
- [50] A. Siani, O.S. Alexeev, G. Lafaye, M.D. Amiridis, The effect of Fe on SiO<sub>2</sub>-supported Pt catalysts: structure, chemisorptive, and catalytic properties, *J. Catal.* 266 (2009) 26–38.
- [51] N.E. Nunez, H.P. Bideberripe, M. Mizrahi, J.M. Ramallo-Lopez, M.L. Casella, G.J. Siri, Co selective oxidation using Co-promoted Pt/ $\gamma$ -Al<sub>2</sub>O<sub>3</sub> catalysts, *Int. J. Hydrogen Energy* 41 (2016) 19005–19013.
- [52] Q. Yu, K.K. Bando, J.-F. Yuan, C.-Q. Luo, A.-P. Jia, G.-S. Hu, J.-Q. Lu, M.-F. Luo, Selective hydrogenation of crotonaldehyde over Ir-FeO<sub>x</sub>/SiO<sub>2</sub> catalysts: enhancement of reactivity and stability by Ir-FeO<sub>x</sub> interaction, *J. Phys. Chem. C* 120 (2016) 8663–8673.
- [53] M. García-Dieguez, I.S. Pieta, M.C. Herrera, M.A. Larrubia, I. Malpartida, L.J. Alemany, Transient study of the dry reforming of methane over Pt supported on different  $\gamma$ -Al<sub>2</sub>O<sub>3</sub>, *Catal. Today* 149 (2010) 380–387.
- [54] G. Corro, C. Cano, J.L.G. Fierro, A study of Pt-Pd/ $\gamma$ -Al<sub>2</sub>O<sub>3</sub> catalysts for methane oxidation resistant to deactivation by sulfur poisoning, *J. Mol. Catal. A Chem.* 315 (2010) 35–42.
- [55] A.P. Grosvenor, B.A. Kobe, M.C. Biesinger, N.S. McIntyre, Investigation of multiplet splitting of Fe 2p XPS spectra and bonding in iron compounds, *Surf. Interface Anal.* 36 (2004) 1564–1574.
- [56] R. Yao, J. Li, P. Wu, X. Li, The superior performance of a Pt catalyst supported on nanoporous SiC-C composites for liquid-phase selective hydrogenation of cinnamaldehyde, *RSC Adv.* 6 (2016) 81211–81218.